

This Work has not yet been peer-reviewed and is provided by the contributing Author(s) as a means to ensure timely dissemination of scholarly and technical Work on a noncommercial basis. Copyright and all rights therein are maintained by the Author(s) or by other copyright owners. It is understood that all persons copying this information will adhere to the terms and constraints invoked by each Author's copyright. This Work may not be reposted without explicit permission of the copyright owner. This work has been submitted to the Journal of Physical Oceanography. Copyright in this work may be transferred without further notice.

Sink of eddy energy by submesoscale sea surface temperature variability in a coupled regional model

Igor Uchoa,^a Jacob Wenegrat,^a Lionel Renault,^b

^a *Department of Atmospheric and Oceanic Science, University of Maryland - College Park*

^b *LEGOS, University of Toulouse, IRD, CNRS, CNES, UPS, Toulouse, France*

Corresponding author: Igor Uchoa, iufarias@umd.edu

8 ABSTRACT: Air-sea interaction impacts ocean energetics via modifications to the exchange of
9 momentum and buoyancy. Prior work at the submesoscale has largely focused on mechanisms
10 related to the eddy kinetic energy (EKE), such as the current feedback on stress, which generates
11 negative wind work, or variations in sea surface temperature (SST) that modify surface winds.
12 However, less is known about the influence of submesoscale SST variability on ocean energetics
13 through its direct effect on the surface flux of available potential energy. In this work, the role of
14 air-sea fluxes on submesoscale ocean energetics is investigated using a fully-coupled model of the
15 California Current region, including a numerical experiment that suppresses the thermal response
16 in the computation of air-sea fluxes at the submesoscale. Correlations between surface buoyancy
17 anomalies and surface buoyancy fluxes lead to an approximately 10–20% loss of submesoscale
18 eddy potential energy (EPE), which results in similar magnitude reductions of the vertical buoyancy
19 production, EKE, and eddy wind work. The changes induced by this mechanism in the energy
20 reservoirs and dissipation/conversion pathways are on the same order of magnitude as the negative
21 wind work induced by the current feedback. A scaling for the EPE flux shows that it is a function
22 of the density ratio and proportional to the surface EPE reservoir of the system. These findings
23 indicate the importance of the submesoscale SST variability, and small-scale variability in surface
24 heat fluxes, in modifying energy reservoirs and conversion pathways of the ocean via the direct
25 flux of EPE at the air-sea interface.

26 SIGNIFICANCE STATEMENT: This work investigates the impact of small oceanic frontal
27 features in the ocean, classified as submesoscale, in the exchange of energy at the air-sea boundary.
28 Submesoscale fronts and filaments range from approximately 0.1 to 10 km and are characterized
29 by strong horizontal density changes and fast-evolving flow. The associated density anomalies at
30 the surface may be important in the overall energy budget of the surface ocean since they can affect
31 the energy fluxes at the air-sea boundary. Two numerical experiments were set up for a comparative
32 analysis of the energy transfer, conversion, and storage in the upper layer of the California Current
33 region. One simulation works as a control experiment with air-sea fluxes calculated using the
34 full-resolution fields. In the second experiment, the role of sea surface temperature anomalies
35 in generating air-sea fluxes is suppressed. A comparison between the two experiments shows a
36 difference of 10-20% in the energy storage and conversion. Sea surface temperature variability may
37 induce a reduction of energy via air-sea fluxes similar to energy dissipation driven by wind-current
38 interactions in the same scale of phenomena.

39 **1. Introduction**

40 The turbulent heat and momentum exchanges across the ocean-atmosphere interface are intrinsi-
41 cally dependent on the scale of the ocean features (Seo et al. 2023). SST variability at the mesoscale
42 plays an essential role in modifying the overlaying atmosphere dynamics, which in turn leads to
43 substantial coupled responses of the ocean (Bishop et al. 2017; Chelton and Xie 2010; O'Neill
44 et al. 2012; Small et al. 2008). However, much of our understanding of how ocean variability leads
45 to coupled interactions is constrained to mesoscale resolution (10-100 km). At smaller scales in
46 the ocean, frontal and filamentous features of the order of 0.1-10 km – denoted submesoscale –
47 are characterized by sharper temperature gradients and ageostrophic flows. Submesoscale currents
48 are common oceanic features driven by the downscale eddy cascade of mesoscale flows and are
49 important to global ocean dynamics (McWilliams 2016; Wenegrat et al. 2018). As the dynamics
50 of submesoscale currents are strongly ageostrophic, strong vertical velocities are characteristic in
51 the flow which allow for significant transport of properties such as dissolved gases, nutrients, and
52 heat (Mahadevan et al. 2012; Renault et al. 2016; Balwada et al. 2021). The vertical flux of heat
53 (buoyancy) affects both the timing and strength of ocean stratification (Mahadevan et al. 2012;

54 Johnson et al. 2016) and the surface flux of heat between the ocean and atmosphere (Su et al. 2018,
55 2020; Iyer et al. 2022).

56 Air-sea interaction at the submesoscale is somewhat less well understood since numerical simu-
57 lations are computationally costly and observations are challenging. Observations of air-sea fluxes
58 at the submesoscale, although scarce, have shown larger fluxes of heat, moisture, and momentum
59 at fronts (Shao et al. 2019; Iyer et al. 2022), also consistent with submesoscale-permitting global
60 ocean models analysis that used uncoupled air-sea bulk formulae (e.g., Su et al. 2018, 2020).
61 Coupled numerical simulations have shown an active EKE transfer at the air-sea interface by sub-
62 mesoscale variations in surface wind stress (e.g., Renault et al. 2018; Bai et al. 2023; Conejero
63 et al. 2024). For example, coupled modeling experiments of the California Current System indicate
64 that modifications to the wind stress by small-scale currents (the current feedback on stress, CFB)
65 lead to a 17% reduction in submesoscale EKE (Renault et al. 2018). These changes to the surface
66 stress also modify the Ekman transport of buoyancy at fronts, and consequently the PV budget
67 of the surface mixed layer (Wenegrat 2023). In addition, modulations of the marine atmospheric
68 boundary layer and changes in atmospheric kinetic energy by SST variability, namely, the thermal
69 feedback mechanism (TFB), were also explored in idealized models (Wenegrat and Arthur 2018;
70 Sullivan et al. 2020, 2021). These results indicate that sharp fronts at the submesoscale impact
71 the response of the marine atmospheric boundary layer by driving secondary circulations in the
72 atmosphere which in turn modify the surface wind stress and wind work (Skylvingstad et al. 2007;
73 Wenegrat and Arthur 2018; Sullivan et al. 2021). Recent studies also show the combined effect
74 of CFB and TFB in the wind stress (Bai et al. 2023; Conejero et al. 2024), which indicates that
75 submesoscale SST variability shows a direct influence on the transfer of momentum between the
76 atmosphere and ocean, modifying the surface flux of EKE.

77 The influence of submesoscale SST variability on ocean energetics through its direct effect on
78 the surface flux of available potential energy (APE), however, is less explored. Observations
79 show strong covariability between surface heat fluxes and surface buoyancy anomalies at the
80 submesoscale (Shao et al. 2019; Iyer et al. 2022; Yang et al. 2024), suggesting there will also be
81 a direct surface flux of submesoscale APE. Using an approximate formulation of APE, i.e., eddy
82 potential energy (EPE, discussed further below), studies have shown that air-sea fluxes contribute
83 to a sink of EPE at the mesoscale (Bishop et al. 2020; Guo et al. 2022), which impacts the baroclinic

84 conversion rate in boundary currents in the first 100 m of the upper ocean (Ma et al. 2016; Renault
85 et al. 2023). However, similar analysis has not yet been explored using submesoscale-permitting
86 models. Here we investigate the impact of SST anomalies on submesoscale APE flux using a fully-
87 coupled regional model of a portion of the California Current system, a region where submesoscale
88 features have been indicated as important drivers of air-sea fluxes of momentum and heat (Capet
89 et al. 2008b; Renault et al. 2018).

90 Two coupled ocean-atmosphere simulation setups are used to assess the effect of submesoscale
91 SST variability on the APE flux, including both a fully coupled simulation and one where sub-
92 mesoscale SST anomalies are not included for air-sea flux calculations. The flux, conversion,
93 and storage components of eddy energy in the mixed layer for both simulations are compared,
94 highlighting an increase of eddy energy when SST anomalies do not affect surface fluxes. The
95 impact of the surface APE flux is not limited to the EPE reservoir but also propagates to changes
96 in EKE through modification of the vertical buoyancy production and changes to the surface wind
97 work. This analysis shows that the flux of APE driven by SST at the submesoscale is comparable
98 in magnitude and effect to analogous transfers of EKE by surface momentum transfer (wind work)
99 at the submesoscale.

100 The work is organized as follows. Section 2 introduces the theoretical background for the eddy
101 energy reservoirs, conversion rates, and fluxes in spectral space and their appropriate approxi-
102 mations. The numerical experiments are described in section 3. In section 4, the submesoscale
103 dynamics of the numerical simulations are described, and the impact of the surface EPE flux is
104 estimated. An approximated form of the EPE flux is obtained and compared with the flux of EKE
105 by the surface wind work in section 5. Finally, the results are summarized in section 6.

106 **2. Definition of energy terms**

107 This work compares the eddy energy pathways and reservoirs of the upper ocean, assessing the
108 influence of submesoscale SST anomalies on air-sea flux variability. We consider the reservoirs,
109 conversion rates, and flux terms of eddy energy in horizontal wavenumber space. The definition
110 of global APE describes this quantity as a volume-conserved subtraction of a background state of
111 minimal energy from the total potential energy of the fluid (Winters et al. 1995). However, if one
112 is interested in the spatial distribution of APE, the local formulation is suited (Roulet and Klein

113 2009; Winters and Barkan 2013; Zemskova et al. 2015). The local APE per unit density is defined
 114 as:

$$APE = \int_{z_r(b)}^z [b - b_r(z')] dz', \quad (1)$$

115 where $b = -g \frac{\rho - \rho_o}{\rho_o}$ is the local buoyancy of the fluid, g is the gravitational acceleration, and ρ_o is
 116 the background surface density. The r subscript denotes a reference buoyancy profile calculated by
 117 spatially resorting density (ρ_r) to a minimal potential energy state, and z_r represents the equilibrium
 118 depth of a water parcel of buoyancy b with respect to b_r (Tseng and Ferziger 2001; Huang 2005;
 119 Stewart et al. 2014).

120 A first-order approximation of (1) can be applied if the displacements between the water parcels
 121 and its equilibrium height, namely $z - z_r$, are sufficiently small and the local reference profile is
 122 approximately linear (Molemaker and McWilliams 2010; Roulet and Klein 2009). This approx-
 123 imate form is often referred as the quasi-geostrophic limit (Lorenz 1955; von Storch et al. 2012;
 124 Stewart et al. 2014) and it is described as follows

$$APE \approx \frac{1}{2} \frac{[b - b_r]^2}{N_r^2}, \quad (2)$$

125 where $N_r^2 = \partial b_r / \partial z$ is the reference squared Brunt-Väisälä frequency. This approximate form—
 126 which we refer to as the eddy potential energy (EPE) for clarity of terminology—has been used
 127 previously for studying both the mesoscale (e.g., Ma et al. 2016; Bishop et al. 2020; Guo et al.
 128 2022), and submesoscale dynamics of the upper ocean (e.g., Callies and Ferrari 2013; Callies et al.
 129 2015; Cao et al. 2021; Yang et al. 2021), and we use it in several places throughout the manuscript.
 130 More details on this formulation of the EPE, as well as the validity of the approximation, are
 131 provided in Appendix A.

132 The reservoirs of EPE and EKE in spectral space are described as follows:

$$EPE = \mathbb{R} \left[\frac{(\widehat{b - b_r}) (\widehat{b - b_r})^*}{2N_r^2} \right], \quad (3)$$

$$EKE = \mathbb{R} \left[\frac{\widehat{u} \widehat{u}^* + \widehat{v} \widehat{v}^*}{2} \right], \quad (4)$$

133 and u and v are the zonal and meridional velocity components. The caret $\widehat{(\cdot)}$ denotes the two-
 134 dimensional Fourier transform. The symbol \mathbb{R} represents the real component of the spectra and the
 135 asterisk (*) indicates the complex conjugate operator. The eddy terms analyzed in this work refer
 136 to the variability encompassed at the small mesoscale and submesoscale horizontal wavenumbers
 137 (see section 3c).

138 The rate of conversion between EPE and EKE, $C_{(EKE,EPE)}$, is

$$C_{(EKE,EPE)} = \mathbb{R}\{\widehat{w}(\widehat{b-b_r})^*\} \quad (5)$$

139 where w represents the vertical velocity component. Conversion of EPE at the submesoscale is
 140 generated by baroclinic mixed-layer instabilities and other ageostrophic secondary circulations that
 141 extract available potential energy from fronts (Fox-Kemper et al. 2008; Wenegrat and McPhaden
 142 2016).

143 APE can be fluxed at the surface when there are correlations between surface buoyancy fluxes
 144 and the reference depth (Scotti and White 2014; Hogg et al. 2013; Zemskova et al. 2015),

$$G_{APE} = -\mathbb{R}\left[\widehat{z_{r_o}}^* \widehat{B_o}\right], \quad (6)$$

145 where z_{r_o} is the equilibrium height of the surface buoyancy and B_o is the net surface buoyancy
 146 flux. The EPE flux likewise takes a similar form (von Storch et al. 2012):

$$G_{EPE} = \mathbb{R}\left[\frac{(\widehat{b_o-b_{r_o}})^* \widehat{B_o}}{N_r^2}\right], \quad (7)$$

147 where b_o and b_{r_o} are the surface buoyancy and surface reference buoyancy, respectively. Negative
 148 $G_{APE/EPE}$ values indicate APE/EPE loss from the ocean, whereas positive $G_{APE/EPE}$ indicates a
 149 gain of APE/EPE.

150 Analogously, the flux of EKE at the surface (or wind work) may be calculated using the surface
 151 boundary conditions for momentum (see Capet et al. 2008b; von Storch et al. 2012). The wind
 152 work, G_{EKE} , is thus defined as

$$G_{EKE} = \frac{1}{\rho_o} \left(\mathbb{R}\left[\widehat{\tau_x} \widehat{u_o}^* + \widehat{\tau_y} \widehat{v_o}^*\right] \right), \quad (8)$$

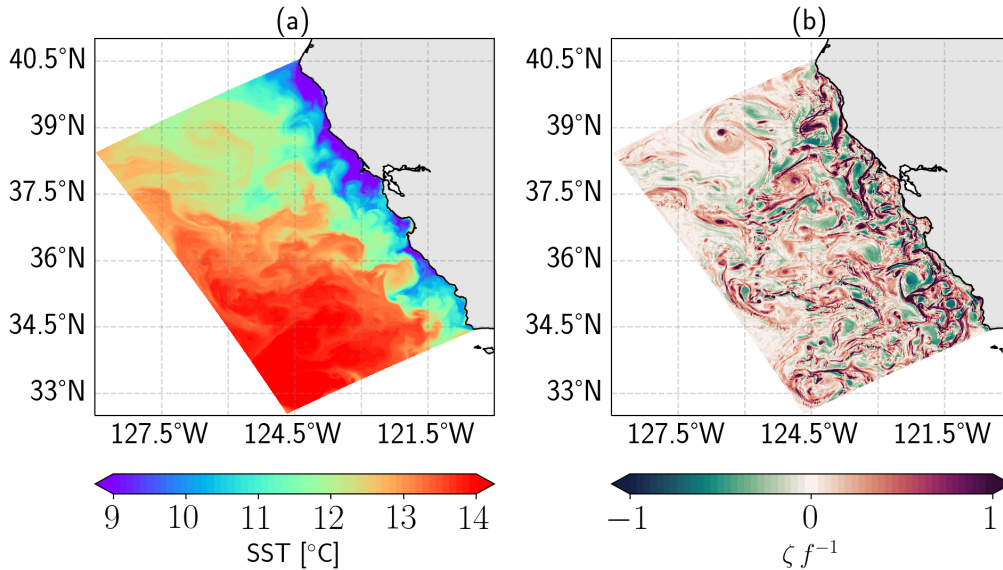
153 where $\boldsymbol{\tau} = (\tau_x, \tau_y)$ is the surface momentum flux vector, and $\mathbf{u}_o = (u_o, v_o)$ is the surface velocity
154 vector.

155 **3. Numerical simulation**

156 *a. Model description*

157 The ocean components of the coupled model in the California Current System region use
158 the Regional Oceanic Modeling System (ROMS) in its CROCO version (Coastal and Regional
159 Oceanic COmmunity) (Shchepetkin and McWilliams 2005; Debreu et al. 2012; Shchepetkin 2015).
160 CROCO is a free-surface, terrain-following coordinate model with split-explicit time stepping.
161 The equations solved in this model's configurations were set for Boussinesq and hydrostatic
162 approximations. The numerical experiments used in this work are the highest resolution products
163 from a four nest configuration described in Renault et al. (2018). The domain for the simulations
164 covers 119.9° W to 128.98° W and from 32.54° N to 40.73° N (Fig. 1). The simulations were spun
165 up from the same initial state from June to November 2011, after which they were run separately
166 from November 2011 to June 2012 (more detailed description in section 3b). The boundary and
167 initial conditions are taken from a coarser 4-km nested grid. For the horizontal grid, 1000×1520
168 points with a grid spacing of $(\Delta x, \Delta y) = 0.5$ km were set with 80 terrain-and-surface-following
169 sigma levels in the vertical with stretching parameters $h_{\text{cline}} = 200$ m, $\theta_b = 3.0$, and $\theta_s = 6$. The
170 turbulence closure used is the K-Profile Parameterization (KPP, Large et al. 1994). The outputs
171 analyzed in this work have a 6-month time span (January to June 2012) with a 6-hour temporal
172 resolution. More information about the settings and spin-up of the model can be found in Renault
173 et al. (2018).

176 For the atmospheric component of the fully-coupled system, the Weather Research and Forecast
177 Model (WRF, version 4.1) was used (Skamarock et al. 2019). An implementation of a nesting grid
178 is also used in this model as in Renault et al. (2018). The atmospheric component used in this work
179 has a spatial resolution of 2 km with initial and boundary conditions provided by the simulation
180 from the previous nesting with a 6 km horizontal resolution. The domain for the simulations covers
181 118.98° W to 129.14° W and from 32.44° N to 41.20° N, which is slightly larger than the ocean
182 domain to avoid the WRF sponge boundaries. For the horizontal grid, 300×390 points with a
183 grid spacing of $(\Delta x, \Delta y) = 2$ km were set with 50 vertical levels. In the boundary layer model,



174 FIG. 1. Snapshots of (a) sea surface temperature and (b) surface vorticity normalized by the Coriolis frequency
 175 (f) from the fully coupled simulation illustrating the model domain.

184 bulk formulae (COARE formulation, Edson et al. 2013) are used to compute the surface turbulent
 185 heat, freshwater, and momentum fluxes, which are subsequently provided to CROCO. Note that
 186 the implementation of a surface-layer vertical mixing parameterization for the planetary boundary
 187 layer (i.e., MYNN, Nakanishi and Niino 2006) and a tri-diagonal matrix for vertical turbulent
 188 diffusion is necessary for the implementation of relative winds in the atmospheric model and to
 189 reproduce the CFB mechanism appropriately (Renault et al. 2019).

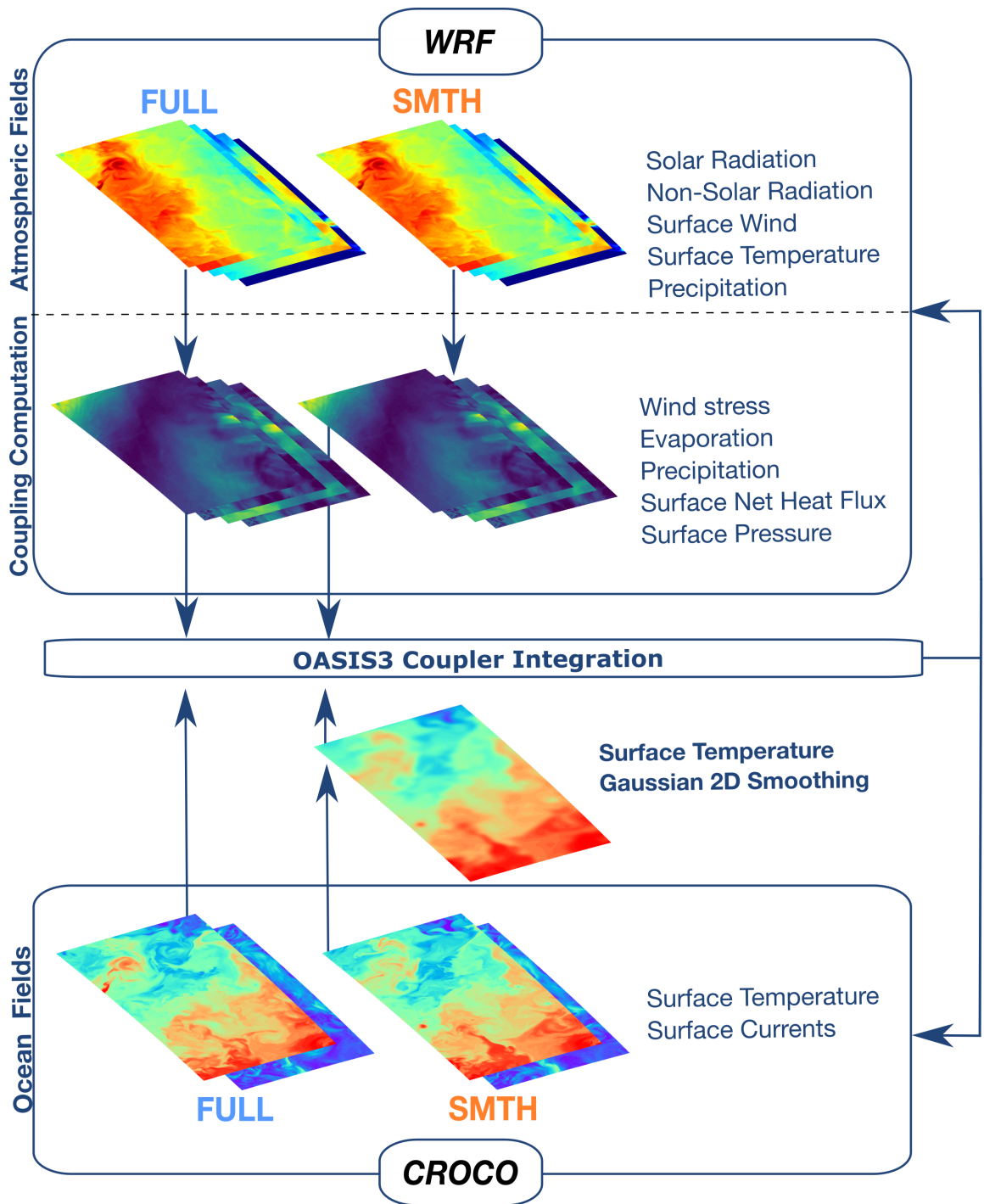
190 The OASIS3 software was used for the surface data exchange between the two models (Valcke
 191 2013) to couple CROCO and WRF. This procedure supports the communication of two-dimensional
 192 fields between the two numerical codes for the integration of the coupled system. The diagram
 193 in Fig. 2 illustrates the surface fluxes computation using this software. In these experiments,
 194 WRF provides the hourly averages of freshwater, heat, and momentum fluxes to CROCO whereas
 195 CROCO feeds the hourly SST and surface currents to WRF for the calculation of fluxes. OASIS3
 196 is implemented in the 4 km and 6 km grids for CROCO and WRF, respectively, and nested into the
 197 higher resolution grids.

198 *b. Experiment setup*

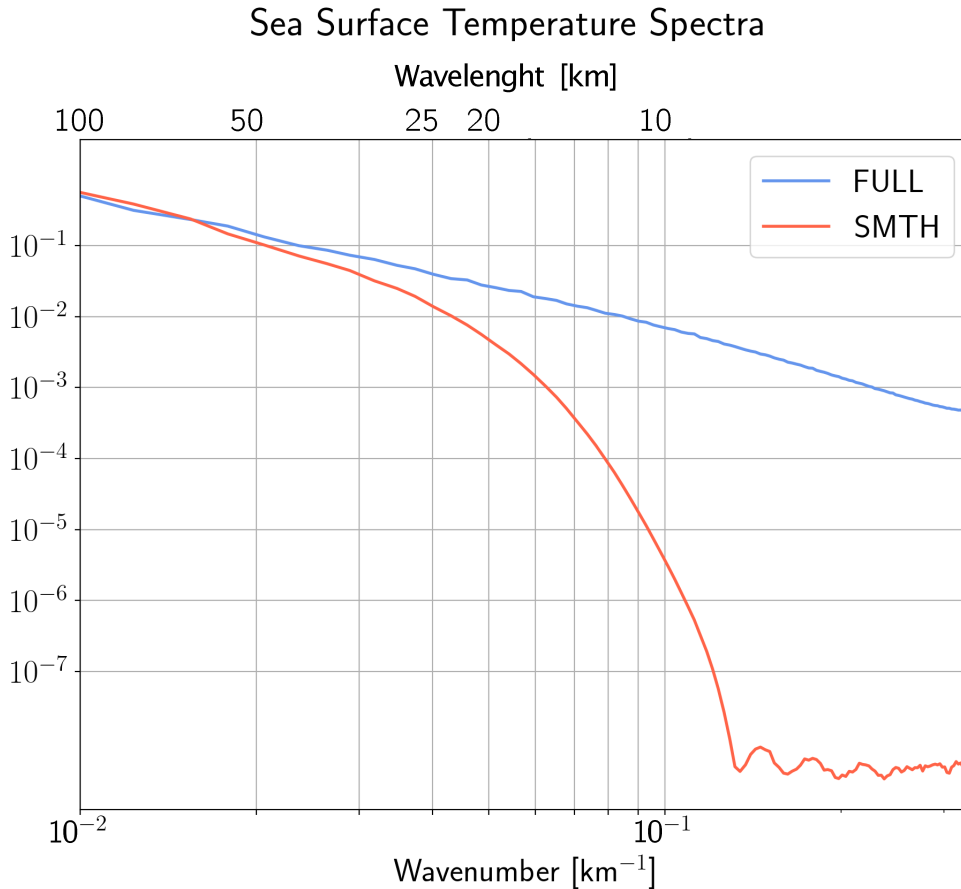
199 To observe the impacts of SST variability at the submesoscale on the upper ocean dynamics,
200 two fully-coupled numerical simulations were implemented using two different air-sea coupling
201 configurations. A schematic of the two experimental setups is illustrated in Fig. 2. The first
202 experiment consists of a fully-coupled model system, hereafter referred to as the FULL experiment.
203 In the second experiment, SST anomalies are low-pass filtered before being passed to WRF for
204 the calculation of surface fluxes, suppressing the role of submesoscale SST variability in air-sea
205 interaction. The latter experiment will be referred to as the SMTH (as in “smooth”) experiment. We
206 emphasize that the model resolution does not change between simulations—the SMTH experiment
207 has the same resolution as FULL (Fig. 2)—the only change is in the resolution of the SST field
208 used in the calculation of surface fluxes. This comparison between experiments thus allows an
209 assessment of the impact of the ocean submesoscale SST variability on the exchange of heat and
210 momentum at the air-sea interface. This analysis is similar to previous studies performed with
211 mesoscale-resolving simulations (Zhai and Greatbatch 2006; Seo et al. 2016; Renault et al. 2023).
212 For more information on the implementation of air-sea coupling in high-resolution models, the
213 reader is referred to Renault et al. (2018, 2019); Jullien et al. (2020).

218 *c. Spatial filtering and spectral analysis*

219 A two-dimensional spatial Gaussian filter is used to isolate submesoscale anomalies from the
220 mesoscale and large-scale signals. The filter applies a $(6\sigma + 1)$ window in both horizontal di-
221 mensions and has a $\sigma=3$ and a cutoff value of 0.5 as performed in Renault et al. (2023). This
222 configuration allows for an assessment of the impact of SST submesoscale anomalies in the energy
223 fluxes, reservoirs, and conversion rates. In Fig. 3 an example of the differences in the SST field
224 used in the air-sea coupling between simulations is shown. The filter reduces variability from
225 approximately 50 km wavelength (0.02 km^{-1} wavenumber) to smaller scales, such that at 20 km
226 wavelength (0.05 km^{-1} wavenumber), SST variability (as seen in the calculation of surface fluxes)
227 is reduced by an order of magnitude. Here we refer to the range of scales smaller than the filter’s
228 largest scale (50 km) as ‘submesoscale’, however we note that the submesoscale is more accurately
229 defined as a dynamical regime, and hence the definition employed here is only approximate. The
230 Fourier transform calculation in this work includes subtraction of the spatial mean and tapering



214 FIG. 2. Schematics of the different coupling computations for the FULL and SMTH experiments using WRF
 215 (The Weather Research and Forecast Model) and CROCO (Coastal and Regional Ocean Community Model). The
 216 examples illustrate the computation of sensible heat flux. The filtering of submesoscale sea surface temperature
 217 variability for the coupling computation is illustrated for the SMTH experiment.



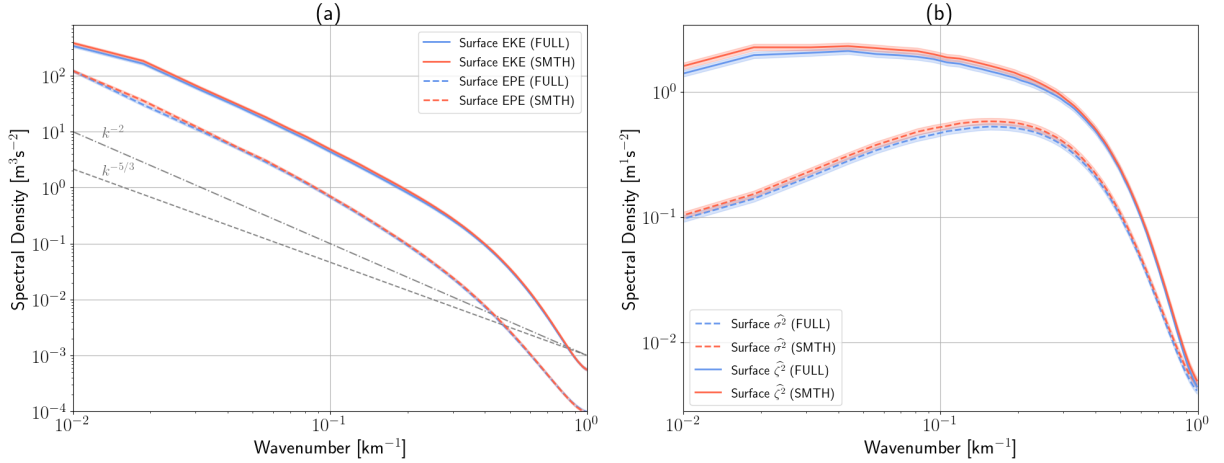
233 FIG. 3. Isotropic wavenumber spectra comparing the sea surface temperature fields strictly used for the coupling
 234 computation of the model simulation setups FULL and SMTH.

231 using a Hanning window. A temporal average of the period of the simulations (i.e., 6 months) is
 232 also applied in all spectra.

235 4. Results

236 a. Model characterization

237 The submesoscale dynamics of the California Current are depicted in Fig. 1 where SST and
 238 normalized relative vorticity fields (i.e., Rossby number) show strong variability in the region.
 239 Smaller-scale vortices and their associated high normalized relative vorticity, $Ro \sim O(1)$, indicate
 240 the presence of flows that are dynamically submesoscale, a consequence of mesoscale strain and
 241 frontal instabilities of the California Current (Capet et al. 2008a).



256 FIG. 4. Surface dynamics and energetics are influenced by air-sea fluxes at the submesoscale. Panel a shows the
 257 two-dimensional spectra of surface eddy kinetic energy (EKE), in solid lines, and the linear approximation of the
 258 available potential energy - the eddy potential energy (EPE)- in dashed lines. Panel b shows surface vorticity (ζ)
 259 in solid lines and divergence (σ) in dashed lines. The shading in each spectrum represents the 95% confidence
 260 interval calculated from a χ^2 distribution using the total number of inertial periods of the experiment's time
 261 period as degrees of freedom. The FULL and SMTH experiments are shown in blue and orange, respectively.

242 The surface eddy energy reservoirs, vorticity, and divergence for the two experiments are shown
 243 in Fig. 4. The SMTH experiment has approximately 5% more EPE and 10% more EKE than the
 244 FULL simulation (Fig. 4a) which suggests an impact from the air-sea fluxes in the surface eddy
 245 energy reservoirs. However, the confidence intervals between experiments overlap even though the
 246 differences between the spectra are consistent at the submesoscale. Greater differences of energy
 247 are found in the fluxes and conversion rates of eddy energy within the mixed layer as discussed
 248 in Section 4d. Both EPE and EKE surface spectra have a slope of $\sim k_h^{-2}$ which is associated with
 249 flows with energetic submesoscale currents (Capet et al. 2008a) and a white horizontal gradient
 250 spectra. The EKE spectral slope found is similar to observations in adjacent regions such as the
 251 Southern California Current (Chereskin et al. 2019), which attributes the behavior to an energetic
 252 submesoscale and relatively weaker mesoscale than in Western Boundary Currents. Vorticity (ζ)
 253 and divergence (δ) spectra are proportional to the horizontal velocity gradient, which indicate sharp
 254 velocity gradients commonly observed in submesoscale fronts and filaments (Barkan et al. 2019).
 255 Fig. 4b indicates weaker velocity gradients in the FULL experiment compared to the SMTH case.

262 *b. Eddy potential energy flux at the submesoscale*

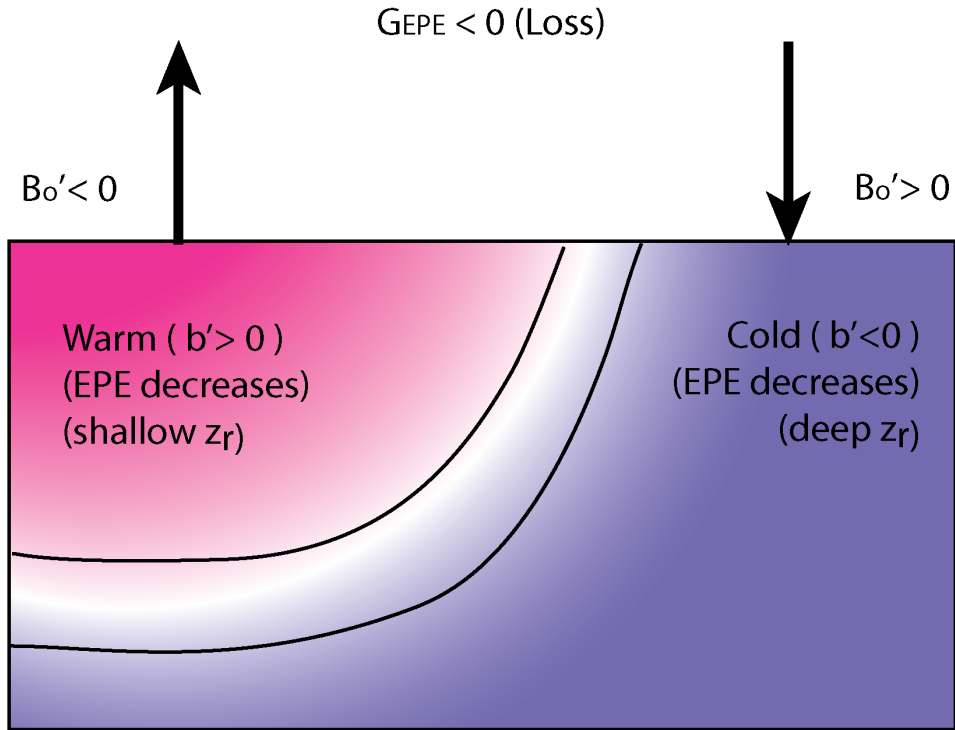
263 SST anomalies at the submesoscale enhance the loss of APE via correlations between the thermal
 264 component of the surface buoyancy flux and the reference level (z_r) of buoyancy anomalies (which
 265 tends to be deeper for cold anomalies and shallower for warm anomalies). Similar also holds
 266 for the approximate form of the APE flux—EPE as described in (2)—where EPE is lost due to
 267 correlations between surface buoyancy anomalies and heat fluxes. A schematic representation of
 268 the mechanism above is shown in Fig. 5 where spatial anomalies of buoyancy (b') and buoyancy
 269 flux (B'_o) are correlated. The heat flux anomalies respond to SST anomalies at the front to diminish
 270 the differences in temperature between the surface ocean and the atmosphere. This mechanism
 271 decreases the absolute values of b' and hence the mixed-layer EPE (assuming temperature anomalies
 272 and buoyancy anomalies are of the same sign, discussed further in section 5).

279 The air-sea buoyancy flux, B_o , may be parameterized as proportional to heat and freshwater
 280 fluxes (Cronin and Sprintall 2001):

$$B_o = \frac{\alpha_\theta g}{\rho_o C_p} Q_{net} - \beta_s g S_o (E - P), \quad (9)$$

281 where g is gravity, S_o is the surface salinity, C_p is the specific heat of water, Q_{net} is the net surface
 282 heat flux, E is evaporation, and P is precipitation. α_θ and β_s represent the thermal expansion and
 283 salinity contraction coefficients calculated at each point. This parameterization allows for the
 284 computation of G_{EPE} .

285 The spectra of G_{APE} and G_{EPE} are shown in Fig. 6. The loss or gain of each to the ocean is
 286 represented as negative and positive spectral density values, respectively. Both the APE flux and
 287 the approximate form, the EPE flux, show differences exceeding an order of magnitude between
 288 the SMTH and FULL experiments. The FULL experiment spectrum shows loss of APE/EPE in the
 289 submesoscale and lower mesoscale spatial range, which indicates that submesoscale APE/EPE flux
 290 acts as a sink of energy to the atmosphere, similar to results found for mesoscale SST anomalies
 291 (von Storch et al. 2012; Bishop et al. 2020; Guo et al. 2022; Renault et al. 2023). Conversely,
 292 the SMTH experiment spectrum indicates a smaller loss of both APE/EPE compared to the FULL
 293 experiment. These differences in surface energy fluxes between the numerical experiments indicate

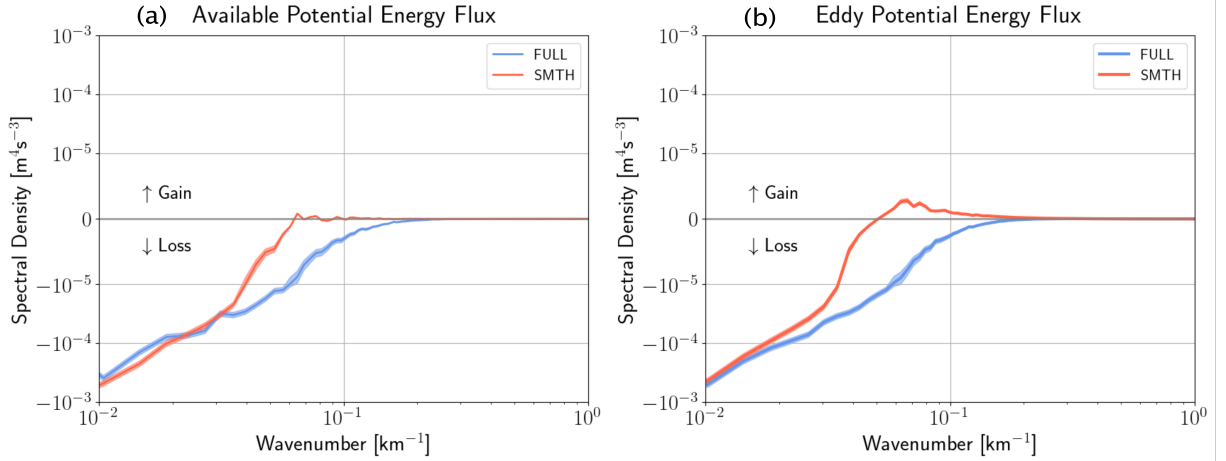


273 FIG. 5. Schematic representation of the surface flux of EPE driven by SST anomalies and heat flux in a
 274 submesoscale front. For simplicity, the buoyancy and buoyancy flux considered in the schematic are treated as
 275 due only to the anomalies in SST and heat flux (salinity contributions are discussed in Section 4c). Heat flux
 276 counteracts the SST anomalies, resulting in a decrease in buoyancy anomaly on both sides of the front and an
 277 overall loss of EPE. This concept can also be applied to the water parcel displacements relative to the surface
 278 (z_r) in both sections of the front. The prime symbol represents the spatial anomalies due to the front.

294 that submesoscale SST variability, and the associated air-sea buoyancy fluxes, act to create a sink
 295 of submesoscale APE.

303 *c. Decomposition of eddy potential energy flux and approximations*

304 It is useful to understand the contributions of temperature and salinity variability and fluxes to
 305 the total flux of APE. This is not straightforward for the exact form of the APE, so here we focus on
 306 the EPE, expanding G_{EPE} to assess the importance of each component contributing to b and B_o
 307 anomalies. To do this, we first approximate the surface buoyancy into a linear equation that takes



296 FIG. 6. Submesoscale buoyancy anomalies are correlated with buoyancy flux anomalies, driving a loss of
 297 EPE (APE) to the atmosphere. Two-dimensional spectra of available potential energy flux for the FULL (blue
 298 line) and SMTH (orange line) experiments. Panel (a) shows the complete computation of the APE flux based on
 299 Zemsanova et al. (2015); Hogg et al. (2013). Panel (b) shows the approximated formulation of APE flux: EPE flux.
 300 The EPE flux spectra show similar variability as the complete formulation of APE flux for the two experiments.
 301 The spectra are averaged over the time period of the simulations. Positive (negative) values represent the gain
 302 (loss) of EPE to the atmosphere. The 95% confidence intervals are represented in the shaded areas.

308 into account SST and salinity anomalies and surface values of α_θ and β_S . The linearized surface
 309 buoyancy in spectral space is:

$$\widehat{b_o - b_{r_o}} \approx g \left[\alpha_\theta \widehat{\Delta T_o} - \beta_S \widehat{\Delta S_o} \right]. \quad (10)$$

310 where $\Delta T_o = T_o - T_{r_o}$ and $\Delta S_o = S_o - S_{r_o}$ are the surface temperature and salinity differences with
 311 respect to the reference state.

312 Using (10) and (9), the EPE flux can be divided into components driven by thermal and salinity
 313 anomalies and fluxes. This decomposition allows for the assessment of the relative contributions
 314 of surface temperature and salinity anomalies and fluxes of heat and freshwater in G_{EPE} . The
 315 expansion can be written as

$$G_{EPE} \approx \frac{1}{N_f^2} \mathbb{R} \left[\widehat{b_T^*} \widehat{B_{oT}} + \widehat{b_T^*} \widehat{B_{oS}} + \widehat{b_S^*} \widehat{B_{oS}} + \widehat{b_S^*} \widehat{B_{oT}} \right], \quad (11)$$

316 where the components of buoyancy and buoyancy flux are defined as follows:

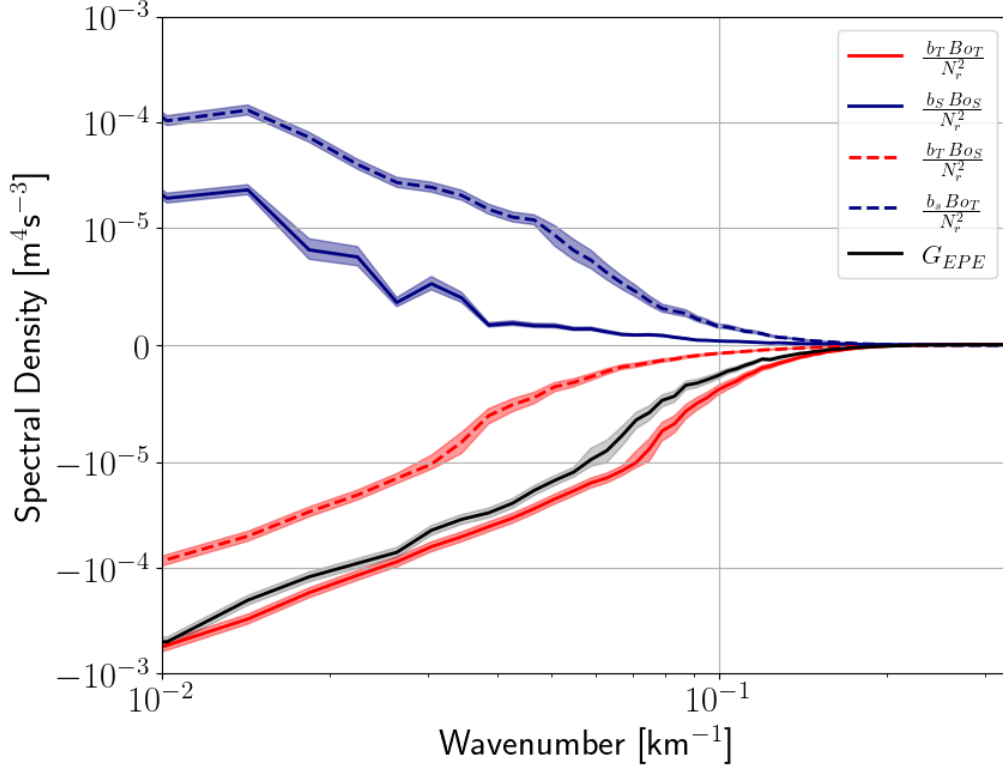
$$\widehat{b}_T = g\alpha_\theta \widehat{\Delta T}_o, \quad (12)$$

$$\widehat{b}_S = -g\beta_S \widehat{\Delta S}_o, \quad (13)$$

$$\widehat{B}_{oT} = \frac{g\alpha_\theta}{\rho_o C_p} \widehat{Q}_{net}, \quad (14)$$

$$\widehat{B}_{oS} = -g\beta_S (\widehat{E} - \widehat{P}) S_o, \quad (15)$$

317 The total EPE flux thus consists of components from (1) direct correlations between surface
 318 temperature anomalies and heat fluxes and surface salinity anomalies and freshwater fluxes and
 319 (2) cross-terms that arise from the correlations between surface heat fluxes (freshwater fluxes) and
 320 salinity anomalies (temperature). The spectra for the four components for the FULL experiments
 321 are shown in Fig. 7. G_{EPE} components related to temperature anomalies (i.e., b_T , Fig. 7 - red
 322 lines) indicate a net loss of EPE to the atmosphere, whereas the components generated by salinity
 323 anomalies (i.e., b_S , Fig. 7 - blue lines) show a net gain of EPE. The product of the thermal
 324 components of buoyancy and buoyancy flux (i.e., $b_T B_{oT}$, Fig. 7 - red solid line) is the dominant
 325 component of EPE flux to the atmosphere at the submesoscale and is responsible for the net loss of
 326 EPE shown in Fig. 6. The term that correlates the salinity component of buoyancy and buoyancy
 327 fluxes (i.e., $b_S B_{oS}$, Fig. 7 - blue solid line) has the smallest magnitude at the submesoscale,
 328 indicating that B_{oS} (proportional to freshwater fluxes) is not as efficient as B_{oT} (proportional to
 329 heat fluxes) in injecting EPE in this region. Instead, the component that contributes to the largest
 330 gain of EPE in the analysis is the cross-term $b_S B_{oT}$ (Fig. 7 - dashed blue line). Temperature and
 331 salinity anomalies drive inverse changes in the EPE of the upper ocean, which as shown below
 332 results from the partial density compensation of fronts in the California Current Region (Rudnick
 333 and Ferrari 1999; Mauzole et al. 2020). B_{oT} may also be further approximated to the latent and
 334 sensible components of heat flux anomalies since those are the components correlated to surface
 335 buoyancy anomalies. This approximation is useful for scaling the EPE flux mechanism and is
 336 explored in the next section.



337 FIG. 7. Decomposition of the total EPE flux (FULL) in terms of the contributions of temperature and salinity
 338 components (see section 4c). Blue lines represent the components of G_{EPE} proportional to salinity anomalies
 339 (b_S). Red lines represent the components proportional to temperature anomalies (b_T). The solid blue and red
 340 lines represent the component proportional to temperature and heat flux anomalies (B_{oT}) and to salinity and
 341 freshwater flux anomalies (B_{oS}). Dashed blue and red lines represent the cross-term components proportional to
 342 temperature and freshwater flux anomalies and to salinity and heat flux anomalies. The black solid line represents
 343 the total sum of the components which accurately explains the total EPE flux term.

344 This analysis suggests the EPE flux in these simulations is well approximated by

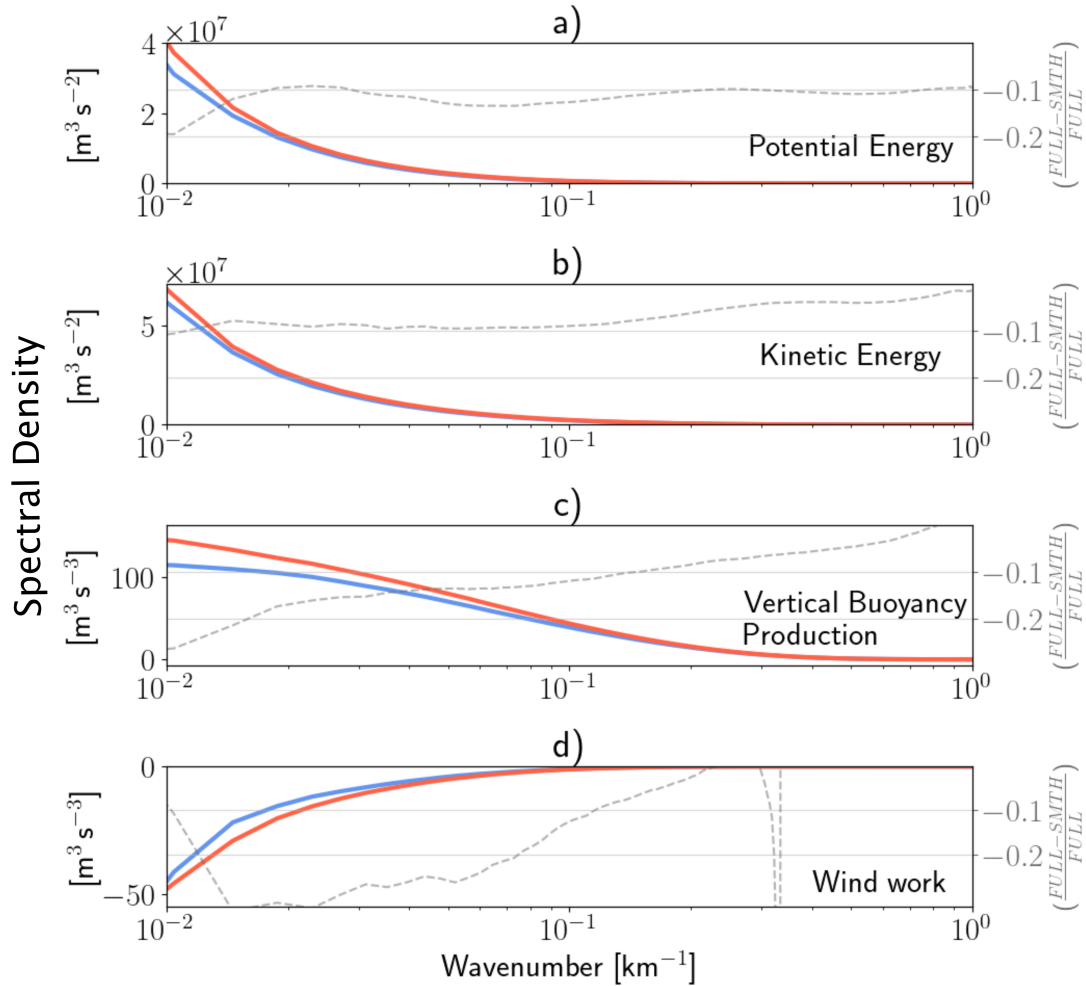
$$G_{EPE} \approx \frac{1}{N_f^2} \mathbb{R} \left[\widehat{b_o^*} \widehat{B_{oT}} \right]. \quad (16)$$

345 In the California Current system, the partial T/S compensation means that while the thermal
 346 component of the buoyancy flux drives a loss of EPE through the temperature anomalies (b_T),
 347 there is also a partially compensating gain of EPE through the correlation of heat flux anomalies
 348 and salinity anomalies (b_S). How the EPE flux depends on density compensation more generally
 349 is discussed further in section 5 below.

350 *d. Eddy energy reservoirs, conversion rates and fluxes*

351 Changes in the EPE flux have impacts on the EPE reservoir but can also affect the EKE through
352 the energy conversion terms. The spectra shown in Fig. 4 suggest that, at the surface, the reservoirs
353 of EPE and EKE are both impacted by the response of SST variability in the air-sea energy transfer
354 via EPE flux. Cumulative spectra (or ogives) of the vertically-integrated reservoirs EKE and EPE
355 in the averaged mixed layer depth (i.e., 50 m using a density threshold of 0.125 kg m^{-3}) are shown
356 in Fig. 8a,b, following similarly to the surface patterns. The EPE flux drives a sink of EPE to
357 the atmosphere due to SST-induced heat flux anomalies (Fig. 6), which generates a reduction of
358 submesoscale EPE in the mixed layer of 10 – 20% (Fig. 8a). At the same scales, EKE is also
359 reduced by approximately 10% as seen in Fig. 8b. The EKE reservoir is likely reduced by the
360 smaller rate of eddy energy conversion, namely, vertical buoyancy production ($C_{(EPE,EKE)}$), which
361 decreases significantly (10 – 25%) in the FULL experiment. As mentioned in section 2, $C_{(EPE,EKE)}$
362 may be attributed to mixed-layer instabilities (and other ageostrophic secondary circulations) where
363 available potential energy stored in thermal-wind balanced fronts is extracted and converted into
364 perturbation flows such as eddies (Capet et al. 2008a; Fox-Kemper et al. 2008) again reflecting the
365 weaker submesoscale in FULL vs. SMTH (Fig. 4). This comparative analysis indicates that at the
366 submesoscale, G_{EPE} directly reduces the EPE which induces a lower baroclinic conversion rate
367 ($C_{EKE,EPE}$) and, consequently, results in a decrease in the EKE reservoir in the mixed layer.

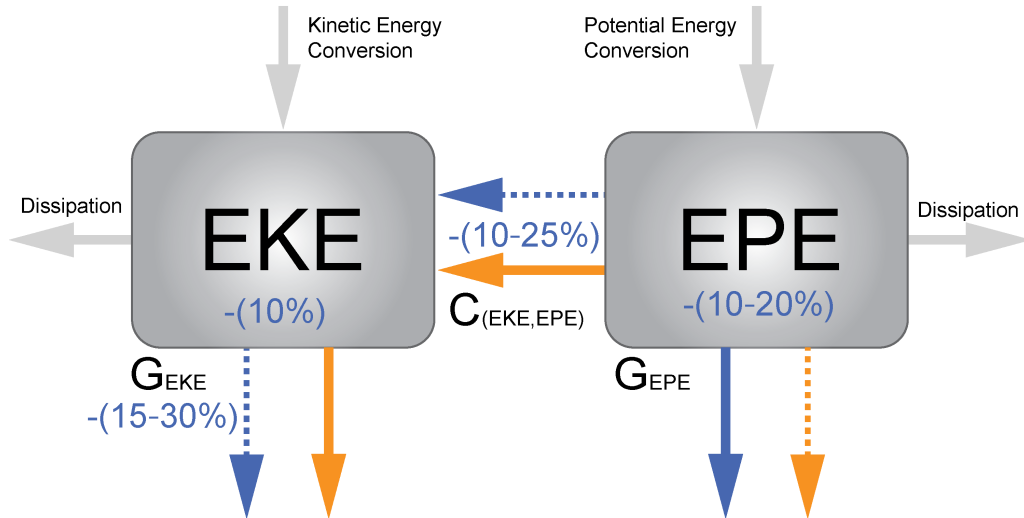
374 Fig. 8d also depicts the cumulative difference in surface EKE flux (G_{EKE}) between the two
375 models. Loss of EKE is present in both experiments at the submesoscale since the CFB effect
376 is accounted for in the wind stress parameterizations. At the submesoscale, there is a relative
377 decrease in wind work in the FULL experiment of 15-30%, a reduction of the EKE flux driven
378 by SST variability. The ratio between the two wind work spectra shown is approximately one or
379 greater than one in scales smaller than the effective resolution of the simulation (approximately 3
380 km as can be inferred from the roll off of the EKE spectra in Fig. 4) and hence these scales are
381 not considered in this analysis. Scalings of the CFB mechanism on the wind work indicate a direct
382 relationship between EKE flux and EKE reservoir in the upper ocean (Renault et al. 2017), which is
383 consistent with the decrease of wind work observed in the less energetic FULL experiment (section
384 5). Concurrently, the TFB mechanism may induce wind anomalies that are partly correlated with
385 surface currents and hence decrease the net loss of EKE by wind work at the submesoscale (Renault



368 FIG. 8. Cumulative spectra of vertically integrated parameters depict the impact of SST variability in air-sea
 369 coupling. Blue (Orange) lines represent the FULL (SMTH) experiment spectra. Ogive graphs are integrated
 370 from the larger to smaller horizontal wavenumber. The panels represent (a) Potential Energy, (b) Kinetic Energy,
 371 (c) vertical buoyancy production, and (d) wind work. Grey dashed lines indicate the relative difference between
 372 the spectra for both experiments. EKE and EPE, and vertical buoyancy production were integrated from 50 m
 373 depth to surface, the averaged mixed-layer depth for the region.

386 et al. 2018; Bai et al. 2023; Conejero et al. 2024; Holmes et al. 2024). This suggests that the more
 387 negative wind work in SMTH experiment is likely due to a combination of the artificial suppression
 388 of TFB and the increase of surface EKE due indirectly to the suppressed EPE flux.

389 A simplified Lorenz diagram summarizing the relative differences in energetics between the two
 390 experiments is depicted in Fig. 9. The vertically-integrated energy fluxes, conversion rates, and



400 FIG. 9. Sea surface temperature variability at the submesoscale alters the pathways and reservoirs of eddy
 401 energy. Simplified Lorenz diagram of the differences in eddy energy reservoirs, fluxes, and conversions. The
 402 FULL (SMTH) experiment is illustrated in blue (orange). Differences between the experiments in each component
 403 are depicted in terms of the FULL spectra decrease. Fluxes of eddy potential energy (i.e., G_{EPE}) and eddy
 404 kinetic energy (i.e., G_{EKE}) are represented by the downward arrows. The reservoirs of eddy potential energy
 405 (i.e., EPE) and eddy kinetic energy (i.e., EKE) are represented by the gray boxes. The conversion of EKE to EPE
 406 (i.e., $C_{EPE,EKE}$) is represented by the horizontal arrows. Grey arrows represent the cross-scale conversions and
 407 dissipation components of energy that are not the focus of this work.

391 reservoirs of both experiments indicate that there is a loss of submesoscale eddy energy in the
 392 upper ocean due to correlations between surface buoyancy anomalies and buoyancy fluxes (Fig.
 393 5). This reduction of EPE then decreases the EKE indirectly through a reduction in the conversion
 394 of EPE to EKE by vertical buoyancy production. Finally, the reduced EKE is associated with a
 395 reduction of CFB wind work, which acts at a rate proportional to the EKE (see section 5). While
 396 the magnitude of these changes in the experiments utilized here are relatively small, $O(10\%)$, they
 397 are similar to changes in the energetics caused by the CFB mechanism found in prior work in this
 398 region (Renault et al. 2018). We discuss the relative importance of these two mechanisms and the
 399 role of temperature and salinity variability and compensation in the following section.

408 5. Discussion

409 In this work, the surface flux of APE is described at the submesoscale, where it facilitates the
410 transfer of energy between the ocean and the atmosphere via correlations between the surface
411 buoyancy flux and the reference level of the surface buoyancy in the adiabatically resorted back-
412 ground profile. Similar is true for the EPE flux which arises from correlations between the surface
413 buoyancy and surface buoyancy fluxes. This mechanism is previously observed using mesoscale-
414 resolving numerical simulations as described in Ma et al. (2016); Bishop et al. (2017); Guo et al.
415 (2022) and Renault et al. (2023), which affects the energy pathways related to conversion rates and
416 reservoirs of eddy energy. The mechanism described in this work highlights the importance of
417 submesoscale SST variability in driving air-sea fluxes at the same scales and how that may affect
418 the estimation of energy conversion rates, sinks, and reservoirs when using numerical simulations.
419 In this section, the limitations of reproducing the EPE flux in numerical models and the importance
420 of this mechanism relative to other air-sea feedbacks are discussed.

421 A hierarchy of coupling parameterizations is used in numerical models in order to reproduce the
422 air-sea fluxes, however some of the strategies may underestimate or even fail to generate surface
423 EPE fluxes. Coupled numerical simulations that use a responsive atmosphere and bulk formulae to
424 reproduce air-sea fluxes that rely on similarity theory (Monin and Obukhov 1954) can reproduce
425 the mechanism studied in this work (e.g., the FULL simulation). Uncoupled models that use
426 a fixed atmosphere, but calculate heat fluxes using parameterizations that depend on SST will
427 likewise generate EPE fluxes, however, it is possible that this flux may not be entirely accurate as
428 the atmosphere cannot evolve in response to these fluxes. However, uncoupled models that use
429 prescribed heat fluxes (a common approach for regional ocean or idealized numerical simulations)
430 fail to generate the mechanism since surface buoyancy fluxes will not respond to surface buoyancy
431 anomalies. In this case, it is anticipated that the modeled submesoscale will be overly energetic
432 (section 4).

433 One of the approximation strategies for air-sea fluxes used in uncoupled ocean-only models relies
434 on the linearization of parameters, such as heat flux, into climatological (background) and local
435 anomalies (perturbation) components. The climatological components in the heat flux can then be
436 prescribed based on available data or reanalyses, whereas the heat flux anomalies are parameterized
437 as proportional to modeled surface temperature anomalies (Barnier et al. 1995; Ma et al. 2016;

438 Moreton et al. 2021). This linearization is particularly amenable to simple implementation in
 439 ocean-only models and may provide a simpler diagnosis of the impact of SST anomalies in the
 440 EPE flux. Here, approximations of the heat flux anomaly as a function of SST are obtained in this
 441 region at the submesoscale. This linearization of the heat flux anomaly as proportional to the SST
 442 anomaly then allows for a further approximation of EPE flux mechanism, described below.

443 For the California Current region, the SST anomalies are mostly correlated to latent and sensible
 444 heat flux anomalies at the submesoscale, explaining over 50% of the variance of those heat flux
 445 components. This allows for the approximation

$$Q'_{net} \approx -\left(Q'_{SH} + Q'_{LH}\right), \quad (17)$$

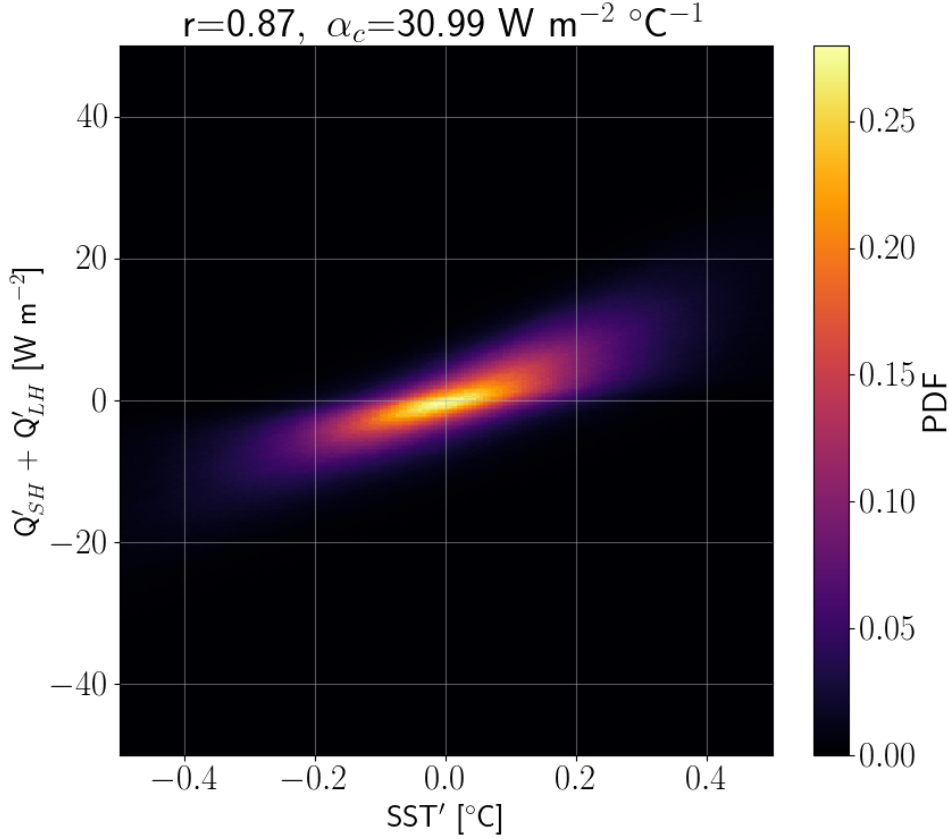
446 where Q'_{SH} and Q'_{LH} are the sensible and latent heat flux components, respectively. The approx-
 447 imation has a negative sign since these turbulent heat flux components are subtracted from the
 448 shortwave heat flux in the Q_{net} computation. The spatial anomalies (') obtained in this analysis are
 449 computed from the subtraction of a spatial low-pass filter, similar to what is applied in the SST field
 450 as described in section 3c, to the variable. Fig. 10 shows the joint probability distribution for SST
 451 and sensible and latent heat flux anomalies over the simulation period. The coupling coefficient α_c
 452 is computed as the linear regression fit slope from the approximated heat flux (17) and SST spatial
 453 anomalies, as shown in Fig. 10. In this work, $\alpha_c=31 \text{ W m}^2\text{ }^\circ\text{C}^{-1}$, which is similar to previous
 454 linearizations for the same region at larger scales (Barnier et al. 1995).

459 As analyzed in section 4b, the correlation between heat flux and surface buoyancy anomalies has
 460 the greatest contribution to the submesoscale EPE flux. By invoking the approximation of EPE
 461 flux in physical space (von Storch et al. 2012) and the linearization of the heat flux obtained in this
 462 work (17), an approximate form of the EPE flux is given by

$$G_{EPE} = -\frac{\alpha_\theta \alpha_c g}{N_r^2 \rho_o C_p} b'_o T'_o. \quad (18)$$

463 This approximation describes EPE flux as the product of surface buoyancy and can also be further
 464 manipulated by approximating buoyancy by the linear equation of state giving

$$G_{EPE} \approx -\frac{1}{N_r^2} \frac{\alpha_C \alpha_\theta^2 g^2}{\rho_o C_p} \left(1 - \frac{1}{R}\right) T_o'^2, \quad (19)$$



455 FIG. 10. Two-dimensional histogram of SST and sensible and latent components of the heat flux (Q_{SH+LH})
 456 anomalies in the FULL simulation setup. The impact of SST anomalies in the EPE flux at the submesoscale may
 457 be linearized using a coupling coefficient derived from anomalies of SST and non-solar heat flux – proportional
 458 to surface buoyancy flux.

465 where R is the surface density ratio defined as:

$$R = \frac{\alpha_\theta T'_o}{\beta_S S'_o}. \quad (20)$$

466 This ratio, R , indicates how temperature and salinity anomalies contribute to the decrease or
 467 increase of buoyancy simultaneously. When $R < 0$, the contribution of temperature and salinity
 468 anomalies to modulate buoyancy are positively correlated. This scenario favors loss of EPE to the
 469 atmosphere as heat flux tends to dissipate buoyancy anomalies (as in Fig. 5), and indeed (21) is
 470 strictly negative for $R < 0$. When $R > 0$, the contribution of temperature and salinity anomaly in

471 buoyancy anomalies are negatively correlated, that is, density compensation occurs (Rudnick and
 472 Ferrari 1999). Observations suggest some degree of density compensation is ubiquitous in regions
 473 with active submesoscales (Rudnick and Martin 2002; Drushka et al. 2019). In compensated fronts,
 474 the sign of G_{EPE} is dependent on the relative magnitude of the thermal and salinity components
 475 of buoyancy in R . If temperature anomalies determine buoyancy anomalies ($R > 1$) then there is
 476 a loss of EPE (as in the simulations here where the median value of the ratio $(1 - R^{-1})^{-1} \approx 0.5$).
 477 Conversely, if the salinity component of buoyancy dominates in a compensated front ($0 < R < 1$),
 478 such that the surface thermal component of buoyancy fluxes act to increase the density anomalies
 479 across the front (i.e., the dense side of the front is associated with warm anomalies that are cooled
 480 by surface heat fluxes), the EPE will increase due to surface fluxes. This suggests that in some
 481 regimes, such as high-latitude β oceans or coastal regions with significant freshwater fluxes, the
 482 EPE flux may act as a source of submesoscale energy.

483 Finally, we note it is also possible to describe G_{EPE} as proportional to the surface EPE reservoir
 484 (detailed derivation in Appendix B)

$$G_{EPE} \approx \frac{1}{(1 - \frac{1}{R})} \frac{2s_b}{\rho_o} EPE_o, \quad (21)$$

485 where $s_b = -\frac{\alpha_c}{C_p}$ [$\text{kg m}^{-2} \text{s}^{-1}$] is the EPE flux coupling coefficient, and EPE_o is the surface
 486 EPE. This form is useful for comparison with the CFB EKE flux, which is proportional to EKE
 487 (Renault et al. 2017). The ratio between the two mechanisms can therefore be scaled as

$$\frac{G_{EPE}}{G_{EKE}} \sim \left(\frac{s_b}{s_\tau}\right) \frac{1}{(1 - \frac{1}{R})} \frac{EPE_o}{EKE_o}, \quad (22)$$

488 where $s_\tau = -3/2\rho_a C_D |U_a|$ is the wind stress coupling coefficient, C_D is the drag coefficient
 489 and $|U_a|$ is the surface wind magnitude. This ratio indicates that the relative impact between
 490 the two mechanisms is a function of: (i) the magnitude of both coupling coefficients, (ii) the
 491 surface density ratio, and (iii) the ratio of the surface eddy energy reservoirs of the system. The
 492 coupling coefficients s_b and s_τ are of similar magnitude considering previous estimates of s_τ using
 493 observations (Renault et al. 2017) and of α_c from computations in this work (Fig. 10).

494 The ratio of EKE_o and EPE_o is scale- and season-dependent due to mesoscale and submesoscale
 495 dynamics. For instance, EKE and EPE spectra of Western Boundary Currents such as the Gulf

496 Stream show that strong baroclinic currents have EKE_o and EPE_o reservoirs of similar magnitude
497 for the winter, whereas in the summer, EKE is larger (Callies et al. 2015). These differences are
498 in part related to mixed-layer instabilities amplified in the wintertime as the mixed-layer depth
499 increases (Fox-Kemper et al. 2008). Observations from the eastern subtropical North Pacific also
500 show EKE and EPE magnitudes to be similar at the mesoscale and submesoscale (Callies and
501 Ferrari 2013). Thus, (22) suggests that the results found here – where the direct EPE flux alters
502 submesoscale energetics in a manner that is quantitatively similar to the surface EKE flux – may be
503 found elsewhere when the EPE_o/EKE_o ratio is large or there is substantial density compensation.

504 **6. Summary and conclusion**

505 In this manuscript, the impact of submesoscale SST variability on the flux of EPE is assessed
506 using two configurations of a fully-coupled model with submesoscale-permitting resolution in the
507 ocean, where one of the numerical experiments (SMTH) suppresses submesoscale SST anomalies
508 in the computation of air-sea fluxes. Comparative analysis between the experiments indicates that
509 modifications to the surface buoyancy flux induced by submesoscale SST variability generate an
510 APE flux at the air-sea interface which acts as a sink of eddy energy in the upper ocean. In these
511 simulations, this leads to a reduction of the EPE reservoir of 10 – 20% at the submesoscale and
512 the small mesoscale. Associated with this, the rate of conversion to EKE by the vertical buoyancy
513 production ($C_{(EPE,EKE)}$) also decreases by 10 – 25%. This in turn leads to an approximately 10%
514 reduction of submesoscale EKE, and consequently a change in the surface wind work (i.e., CFB;
515 Renault et al. 2018) of 15 – 30%. These changes to submesoscale energy are similar in magnitude
516 to those induced in the same region by the CFB, as well as at larger scales globally (Renault et al.
517 2018; Bishop et al. 2020).

518 Linearizations of the turbulent heat flux as a function of SST perturbations at the submesoscale
519 (coupling coefficient α_c) allow for the scaling of the EPE flux at the submesoscale in terms of
520 surface buoyancy and temperature anomalies. The EPE flux may then be described as a function of
521 the surface EPE, analogous to scaling arguments for EKE flux being proportional to EKE reservoir
522 (Renault et al. 2017, 2018), with relative magnitude also dependent on the degree of density
523 compensation (Rudnick and Ferrari 1999). A ratio between the EPE and EKE fluxes results in
524 a term proportional to the ratio between the eddy energy reservoirs, suggesting that the relative

525 importance of the EPE flux and CFB mechanisms in reducing eddy energy will be dependent on the
526 relative sizes of the surface EPE and EKE. In this work considering the California Current region,
527 the EPE flux is a sink of surface EPE at the same magnitude of the CFB mechanism for surface
528 EKE, despite the counteracting effect of the partial salinity compensation found in this region (eg.,
529 Fig. 7). In regions where salinity dominates in the density compensation (e.g., $0 < R < 1$ as found
530 at high latitudes or regions with strong freshwater influence), EPE flux may contribute to a gain of
531 EPE hence energizing the submesoscale.

532 We note that changes between simulations at scales larger than the SST filter scale were also
533 observed in these experiments, which could indicate a change in the upscale flux of energy
534 from the submesoscale to the mesoscale. This suggests the possibilities of non-linear effects
535 not captured in our current interpretation of results (section 4). However, the limited domain
536 size and integration time period of the numerical model considered here do not allow a robust
537 characterization of changes at larger scales. Looking forward, a scale-dependent APE budget
538 study using a submesoscale-resolving experiment in a larger domain would provide useful insight
539 into both the direct and cross-scale effects of the surface energy fluxes and conversion rates.
540 Likewise, extensions of this work to also include additional experiments with spatial filtering
541 of surface currents, near-surface surface winds, or near-surface atmospheric temperature would
542 provide additional insight into how fine-scale variability on each side of the air-sea interface impacts
543 the energetics and dynamics of the ocean.

544 *Acknowledgments.* This work is a contribution to the S-MODE project (Farrar et al. 2020), an
545 EVS-3 Investigation awarded under NASA Research Announcement NNH17ZDA001N-EVS3 and
546 NASA grants 80NSSC21K0554 and 80NSSC24K0412 awarded under NASA Research Announce-
547 ment NNH20ZDA001NPO to the University of Maryland, College Park. This work also used the
548 GENCI (project 13051) computing resources and support from I-CASCADE, POSEIDON-SWOT,
549 and M-ODYSEA TOSCA-CNES projects.

550 *Data availability statement.* No observational data was used in this work. Analysis scripts will
551 be made available via <http://github.com> upon publication.

552 APPENDIX A

553 Available potential energy approximation for mixed-layer submesoscale dynamics

554 In this appendix we first briefly review the origin of the approximate form of the available potential
555 energy (APE) used, and then briefly discuss the validity of that approximation for considering
556 surface APE at the submesoscale in our simulations. The APE describes the portion of potential
557 energy that can be adiabatically converted to kinetic energy. Its definition arises from the volume-
558 conserved subtraction of the total potential energy (i.e., $\rho_o z b$) and the background potential energy
559 (i.e., $\rho_o z_r b$), related to the minimum state of energy for the fluid (Winters et al. 1995; Winters
560 and Barkan 2013; Scotti and Passaglia 2019). The buoyancy reference profile and associated
561 displacements are here calculated on every time snapshot of the model with a topography-sensitive
562 single basin resorting method based on Huang (2005); Tseng and Ferziger (2001); Stewart et al.
563 (2014).

564 A local definition of the APE density is given by (Holliday and McIntyre 1981; Roulet and Klein
565 2009),

$$APE(z, b) = \int_{z_r(b)}^z [b - b_r(z')] dz', \quad (\text{A1})$$

566 which has a volume integral equal to the global APE (Molemaker and McWilliams 2010). Although
567 the local APE is positive definite, it is not quadratic as it includes higher-order terms in its
568 computation.

569 The approximation of the local APE is given by simplifying the integral of Eq. A1, assum-
570 ing small curvature of the reference buoyancy profile, b_r , over the scales of the water parcel
571 displacements when reordering. It is then approximated as,

$$APE(z, b) \approx g [z - z_r(b)] \frac{[2b - b_r(z) - b_r(z_r)]}{2}. \quad (\text{A2})$$

572 Since z_r is the inverse mapping of b_r , $b_r(z_r) = b$, and

$$APE(z, b) \approx g [z - z_r(b)] \frac{[b - b_r(z)]}{2}. \quad (\text{A3})$$

573 Linearizing z_r for a fixed b using a first-order Taylor expansion and again assuming the water
574 parcel displacements to be small (Roulet and Klein 2009), z_r becomes:

$$z_r(b) \approx z_r(b_r) + [b - b_r] \frac{\partial z_r}{\partial b} \Big|_{b_r} \quad (\text{A4})$$

575 By manipulating A4, an expression for the water parcel displacement for a fixed b is obtained:

$$z - z_r(b) \approx \frac{[b - b_r]}{N_r^2(z)}. \quad (\text{A5})$$

576 Applying Eq. A5 in Eq. A3, gives the approximate form (which we refer to as the Eddy Potential
577 Energy (EPE) for clarity of terminology),

$$APE(z, b) \approx EPE(z, b) := \frac{[b - b_r]^2}{2N_r^2}. \quad (\text{A6})$$

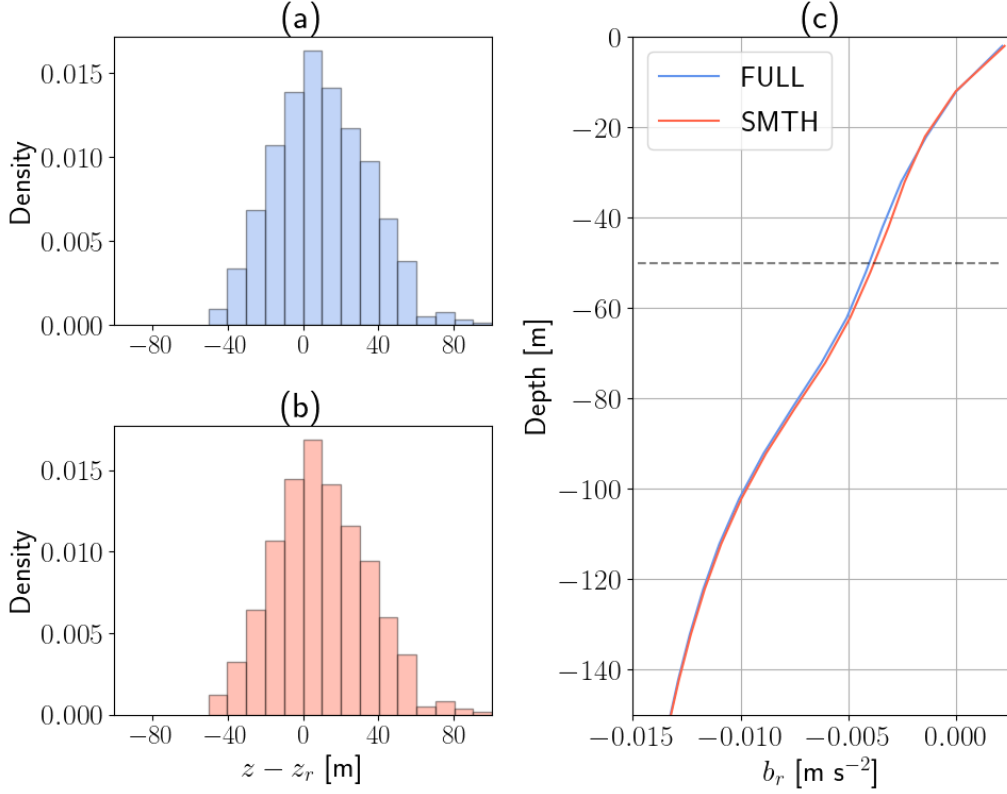
578 The APE and EPE are then each also associated with slightly different forms of the surface flux, as
579 discussed in section 2.

580 This approximation to the APE is common in studies of the submesoscale due to its computational,
581 and conceptual, simplicity (e.g. Callies and Ferrari 2013; Callies et al. 2015; Cao et al. 2021;
582 Yang et al. 2021). A full assessment of the limitations of the EPE approximation to APE at
583 the submesoscale is beyond the scope of this work, however we do note that because of the
584 small buoyancy variance at the submesoscale (relative to larger scales), the vertical displacements
585 associated with resorting submesoscale surface buoyancy anomalies are small (fig. A1). Further,
586 over these depth ranges the reference buoyancy profile has limited curvature (as opposed to deeper
587 in the permanent pycnocline). Hence, the assumptions used in reaching the EPE (small $z - z_r$, and
588 limited curvature of the reference buoyancy profile) may be reasonable at these scales, at least in
589 the simulation considered here. Regardless, we emphasize that the approximate form is only used
590 in a limited sense in this manuscript: as an approximation for quantifying the ‘reservoir’ of APE
591 in wavenumber space, and for determining the relative contributions of salinity and temperature
592 variations and fluxes to the total APE flux. The primary results of the manuscript—submesoscale
593 SST variability inducing fluxes of APE that alter conversion of APE to EKE and surface wind
594 work—are independent of this approximation.

600 APPENDIX B

601 **Approximated form of the EPE flux at the submesoscale**

602 The EPE flux is defined as the product of the surface buoyancy and the buoyancy flux anomalies
603 as follows (Bishop et al. 2020; von Storch et al. 2012):



595 FIG. A1. Small displacements ($z - z_r$) of parcels from their equilibrium height and linear reference density
 596 profiles in the mixed layer indicate linear dominance in the local APE density. Panels a,b depict the histogram of
 597 displacements between the in the averaged mixed-layer depth. Panel c shows the time-averaged reference profile
 598 of buoyancy (b_r). The gray dashed line represents the averaged mixed-layer depth. Blue colors indicate FULL
 599 experiment, and red colors indicate SMTH.

$$G_{EPE} = \frac{b'_o B'_o}{N_r^2}, \quad (\text{B1})$$

604 where b'_o and B'_o are defined respectively as:

$$b'_o = \alpha_\theta g T'_o - \beta_s g S'_o, \quad (\text{B2})$$

$$B'_o = \frac{\alpha_\theta g}{\rho_o C_p} Q'_{net} - \beta_s g S'_o [E' - P'], \quad (\text{B3})$$

605 where the prime symbol (') denotes the anomaly of a given variable. It is convenient to describe
 606 surface buoyancy perturbations in terms of temperature as follows:

$$b'_o = \alpha_\theta g T'_o \left(1 - \frac{1}{R}\right), \quad (\text{B4})$$

607 where R is the density ratio (defined in (20) and see also Rudnick and Ferrari 1999). Since at the
 608 submesoscale, the EPE flux from the ocean to the atmosphere is primarily generated by surface
 609 heat flux anomalies (Fig. 7), we can combine (B4) and (B3) in (B1) to yield

$$G_{EPE} \approx \frac{1}{N_r^2} \frac{\alpha_\theta^2 g^2}{\rho_o C_p} \left(1 - \frac{1}{R}\right) T'_o Q'_{net}. \quad (\text{B5})$$

610 As described in section 5, it is further possible to approximate the correlated component of the
 611 heat flux anomaly in terms of a coupling coefficient. Q'_{net} may then be described as

$$Q'_{net} \approx -\alpha_C T'_o \quad (\text{B6})$$

612 Thus G_{EPE} is approximately:

$$G_{EPE} \approx -\frac{1}{N_r^2} \frac{\alpha_C \alpha_\theta^2 g^2}{\rho_o C_p} \left(1 - \frac{1}{R}\right) T_o'^2. \quad (\text{B7})$$

613 Using the definition of eddy potential energy (EPE) in terms of density ratio:

$$EPE_o = \frac{1}{2} \frac{\alpha_\theta^2 g^2}{N_r^2} \left(1 - \frac{1}{R}\right)^2 T_o'^2 \quad (\text{B8})$$

614 and multiplying the term $(1 - \frac{1}{R})$ in the numerator and denominator of (B7), the equation can be
 615 manipulated further in terms of $b_o'^2$. Thus, (B7) becomes:

$$G_{EPE} \approx \frac{1}{\left(1 - \frac{1}{R}\right)} \frac{2s_b}{\rho_o} EPE_o, \quad (\text{B9})$$

616 where $s_b = -\alpha_C/C_p \text{ kg m}^{-2} \text{ s}^{-1}$.

617 This takes a form similar to the current feedback effect on the wind work, which can be expressed
618 as (Renault et al. 2017):

$$G_{EKE} \approx \frac{2s_\tau}{\rho_o} EKE_o, \quad (\text{B10})$$

619 where $s_\tau \approx -3/2\rho_a C_D |U_a| \text{ [kg m}^{-2} \text{ s}^{-1}]$. Notably, both G_{EPE} and G_{EKE} can thus be seen to
620 act as linear damping terms in the potential and kinetic energy equations, respectively. The ratio
621 between EPE and EKE flux at the submesoscale is

$$\frac{G_{EPE}}{G_{EKE}} \sim \frac{2\alpha_C}{3\rho_a C_D C_p |U_a|} \frac{1}{(1 - \frac{1}{R})} \frac{EPE_o}{EKE_o}. \quad (\text{B11})$$

622 References

- 623 Bai, Y., A. F. Thompson, A. B. V. Bôas, P. Klein, H. S. Torres, and D. Menemenlis, 2023:
624 Sub-mesoscale wind-front interactions: The combined impact of thermal and current feedback.
625 *Geophysical Research Letters*, **50**, <https://doi.org/10.1029/2023GL104807>.
- 626 Balwada, D., Q. Xiao, S. Smith, R. Abernathy, and A. R. Gray, 2021: Vertical fluxes conditioned
627 on vorticity and strain reveal submesoscale ventilation. *Journal of Physical Oceanography*,
628 **51** (9), 2883–2901.
- 629 Barkan, R., M. J. Molemaker, K. Srinivasan, J. C. McWilliams, and E. A. D’Asaro, 2019: The
630 role of horizontal divergence in submesoscale frontogenesis. *Journal of Physical Oceanography*,
631 **49** (6), 1593–1618.
- 632 Barnier, B., L. Siefridt, and P. Marchesiello, 1995: Thermal forcing for a global ocean circulation
633 model using a three-year climatology of ECMWF analyses. *Journal of Marine Systems*, **6**,
634 363–380.
- 635 Bishop, S. P., R. J. Small, and F. O. Bryan, 2020: The global sink of available potential en-
636 ergy by mesoscale air-sea interaction. *Journal of Advances in Modeling Earth Systems*, **12**,

637 <https://doi.org/10.1029/2020MS002118>.

638 Bishop, S. P., R. J. Small, F. O. Bryan, and R. A. Tomas, 2017: Scale dependence of midlatitude air-
639 sea interaction. *Journal of Climate*, **30**, 8207–8221, <https://doi.org/10.1175/JCLI-D-17-0159.1>.

640 Callies, J., and R. Ferrari, 2013: Interpreting energy and tracer spectra of upper-ocean turbulence
641 in the submesoscale range (1–200 km). *Journal of Physical Oceanography*, **43**, 2456–2474,
642 <https://doi.org/10.1175/JPO-D-13-063.1>.

643 Callies, J., R. Ferrari, J. M. Klymak, and J. Gula, 2015: Seasonality in submesoscale turbulence.
644 *Nature Communications*, **6**, <https://doi.org/10.1038/ncomms7862>.

645 Cao, H., B. Fox-Kemper, and Z. Jing, 2021: Submesoscale eddies in the upper ocean of the kuroshio
646 extension from high-resolution simulation: Energy budget. *Journal of Physical Oceanography*,
647 <https://doi.org/10.1175/jpo-d-20-0267.1>.

648 Capet, X., J. C. McWilliams, M. J. Molemaker, and A. F. Shchepetkin, 2008a: Mesoscale to
649 submesoscale transition in the California Current system. Part I: Flow structure, eddy flux,
650 and observational tests. *Journal of Physical Oceanography*, **38**, 29–43, [https://doi.org/10.1175/](https://doi.org/10.1175/2007JPO3671.1)
651 [2007JPO3671.1](https://doi.org/10.1175/2007JPO3671.1).

652 Capet, X., J. C. McWilliams, M. J. Molemaker, and A. F. Shchepetkin, 2008b: Mesoscale to
653 submesoscale transition in the California Current system. Part II: Frontal processes. *Journal of*
654 *Physical Oceanography*, **38**, 44–64, <https://doi.org/10.1175/2007JPO3672.1>.

655 Chelton, D. B., and S. P. Xie, 2010: Coupled ocean-atmosphere interaction at oceanic mesoscales.
656 *Oceanography*, **23**, 54–69, <https://doi.org/10.5670/oceanog.2010.05>.

657 Chereskin, T. K., C. B. Rocha, S. T. Gille, D. Menemenlis, and M. Passaro, 2019: Characterizing
658 the transition from balanced to unbalanced motions in the southern California Current. *Journal*
659 *of Geophysical Research: Oceans*, **124** (3), 2088–2109.

660 Conejero, C., L. Renault, F. Desbiolles, J. McWilliams, and H. Giordani, 2024: Near-surface
661 atmospheric response to meso-and submesoscale current and thermal feedbacks. *Journal of*
662 *Physical Oceanography*.

- 663 Cronin, M., and J. Sprintall, 2001: Wind and buoyancy-forced upper ocean. *Encyclopedia of Ocean*
664 *Sciences*, 3219–3226, <https://doi.org/10.1006/rwos.2001.0157>.
- 665 Debreu, L., P. Marchesiello, P. Penven, and G. Cambon, 2012: Two-way nesting in split-explicit
666 ocean models: Algorithms, implementation and validation. *Ocean Modelling*, **49**, 1–21.
- 667 Drushka, K., W. E. Asher, J. Sprintall, S. T. Gille, and C. Hoang, 2019: Global patterns of
668 submesoscale surface salinity variability. *Journal of Physical Oceanography*, **49** (7), 1669–
669 1685.
- 670 Edson, J. B., and Coauthors, 2013: On the exchange of momentum over the open ocean. *Journal*
671 *of Physical Oceanography*, **43** (8), 1589–1610.
- 672 Farrar, J. T., and Coauthors, 2020: S-MODE: The Sub-Mesoscale Ocean Dynamics Experiment.
673 *IGARSS 2020-2020 IEEE international geoscience and remote sensing symposium*, IEEE, 3533–
674 3536.
- 675 Fox-Kemper, B., R. Ferrari, and R. Hallberg, 2008: Parameterization of mixed layer eddies. Part
676 I: Theory and diagnosis. *Journal of Physical Oceanography*, **38**, 1145–1165, [https://doi.org/](https://doi.org/10.1175/2007JPO3792.1)
677 [10.1175/2007JPO3792.1](https://doi.org/10.1175/2007JPO3792.1).
- 678 Guo, Y., S. Bishop, F. Bryan, and S. Bachman, 2022: A global diagnosis of eddy potential
679 energy budget in an eddy-permitting ocean model. *Journal of Physical Oceanography*, **52** (8),
680 1731–1748.
- 681 Hogg, A. M., H. A. Dijkstra, and J. A. Saenz, 2013: The energetics of a collapsing meridional
682 overturning circulation. *Journal of Physical Oceanography*, **43**, 1512–1524, [https://doi.org/](https://doi.org/10.1175/JPO-D-12-0212.1)
683 [10.1175/JPO-D-12-0212.1](https://doi.org/10.1175/JPO-D-12-0212.1).
- 684 Holliday, D., and M. E. McIntyre, 1981: On potential energy density in an incompressible, stratified
685 fluid. *Journal of Fluid Mechanics*, **107**, 221–225, <https://doi.org/10.1017/S0022112081001742>.
- 686 Holmes, R. M., L. Renault, L. Maillard, and J. Boucharel, 2024: Air-sea coupling feedbacks over
687 tropical instability waves. *Journal of Physical Oceanography*.
- 688 Huang, R. X., 2005: Available potential energy in the world's oceans. *Journal of Marine Research*,
689 **63** (1), 141–158.

- 690 Iyer, S., K. Drushka, E. J. Thompson, and J. Thomson, 2022: Small-scale spatial variations of
691 air-sea heat, moisture, and buoyancy fluxes in the tropical trade winds. *Journal of Geophysical*
692 *Research: Oceans*, **127**, <https://doi.org/10.1029/2022JC018972>.
- 693 Johnson, L., C. M. Lee, and E. A. D’Asaro, 2016: Global estimates of lateral spring-
694 time restratification. *Journal of Physical Oceanography*, **46**, 1555–1573, [https://doi.org/](https://doi.org/10.1175/JPO-D-15-0163.1)
695 [10.1175/JPO-D-15-0163.1](https://doi.org/10.1175/JPO-D-15-0163.1).
- 696 Jullien, S., S. Masson, V. Oerder, G. Samson, F. Colas, and L. Renault, 2020: Impact of ocean-
697 atmosphere current feedback on ocean mesoscale activity: Regional variations and sensitivity
698 to model resolution. *Journal of Climate*, **33** (7), 2585–2602.
- 699 Large, W. G., J. C. McWilliams, and S. C. Doney, 1994: Oceanic vertical mixing: A review and a
700 model with a nonlocal boundary layer parameterization. *Reviews of geophysics*, **32** (4), 363–403.
- 701 Lorenz, E. N., 1955: Available potential energy and the maintenance of the general circulation.
702 *Tellus*, **7** (2), 157–167.
- 703 Ma, X., and Coauthors, 2016: Western boundary currents regulated by interaction between ocean
704 eddies and the atmosphere. *Nature*, **535**, 533–537, <https://doi.org/10.1038/nature18640>.
- 705 Mahadevan, A., E. D. . Asaro, C. Lee, and M. J. Perry, 2012: Eddy-driven stratification initiates
706 North Atlantic spring phytoplankton blooms. *Science*, **337**, 54–58, URL [https://www.science.](https://www.science.org)
707 [org](https://www.science.org).
- 708 Mauzole, Y., H. Torres, and L.-L. Fu, 2020: Patterns and dynamics of SST fronts in the California
709 Current System. *Journal of Geophysical Research: Oceans*, **125** (2), e2019JC015499.
- 710 McWilliams, J. C., 2016: Submesoscale currents in the ocean. *Proceedings of the Royal Society*
711 *A: Mathematical, Physical and Engineering Sciences*, **472** (2189), 20160117.
- 712 Molemaker, M. J., and J. C. McWilliams, 2010: Local balance and cross-scale flux of avail-
713 able potential energy. *Journal of Fluid Mechanics*, **645**, 295–314, [https://doi.org/10.1017/](https://doi.org/10.1017/S0022112009992643)
714 [S0022112009992643](https://doi.org/10.1017/S0022112009992643).

- 715 Monin, A., and A. Obukhov, 1954: Osnovnye zakonomernosti turbulentnogo peremeshivaniya v
716 prizemnom sloe atmosfery (Basic laws of turbulent mixing in the atmosphere near the ground).
717 *Trudy geofiz. inst. AN SSSR*, **24 (151)**, 163–187.
- 718 Moreton, S., D. Ferreira, M. Roberts, and H. Hewitt, 2021: Air-sea turbulent heat flux feedback over
719 mesoscale eddies. *Geophysical Research Letters*, **48**, <https://doi.org/10.1029/2021GL095407>.
- 720 Nakanishi, M., and H. Niino, 2006: An improved Mellor–Yamada level-3 model: Its numerical
721 stability and application to a regional prediction of advection fog. *Boundary-Layer Meteorology*,
722 **119**, 397–407.
- 723 O’Neill, L. W., D. B. Chelton, and S. K. Esbensen, 2012: Covariability of surface wind and stress
724 responses to sea surface temperature fronts. *Journal of Climate*, **25**, 5916–5942, [https://doi.org/](https://doi.org/10.1175/JCLI-D-11-00230.1)
725 [10.1175/JCLI-D-11-00230.1](https://doi.org/10.1175/JCLI-D-11-00230.1).
- 726 Renault, L., C. Deutsch, J. C. McWilliams, H. Frenzel, J.-H. Liang, and F. Colas, 2016: Partial
727 decoupling of primary productivity from upwelling in the California Current system. *Nature*
728 *Geoscience*, **9 (7)**, 505–508.
- 729 Renault, L., F. Lemarié, and T. Arsouze, 2019: On the implementation and consequences of
730 the oceanic currents feedback in ocean–atmosphere coupled models. *Ocean Modelling*, **141**,
731 101–123.
- 732 Renault, L., S. Masson, V. Oerder, F. Colas, and J. C. McWilliams, 2023: Modulation of the
733 oceanic mesoscale activity by the mesoscale thermal feedback to the atmosphere. *Journal of*
734 *Physical Oceanography*, **53**, 1651–1667.
- 735 Renault, L., J. C. McWilliams, and J. Gula, 2018: Dampening of submesoscale currents by
736 air-sea stress coupling in the Californian upwelling system. *Scientific Reports*, **8**, [https://doi.org/](https://doi.org/10.1038/s41598-018-31602-3)
737 [10.1038/s41598-018-31602-3](https://doi.org/10.1038/s41598-018-31602-3).
- 738 Renault, L., J. C. McWilliams, and S. Masson, 2017: Satellite observations of imprint of
739 oceanic current on wind stress by air-sea coupling. *Scientific Reports*, **7**, [https://doi.org/](https://doi.org/10.1038/s41598-017-17939-1)
740 [10.1038/s41598-017-17939-1](https://doi.org/10.1038/s41598-017-17939-1).

- 741 Roullet, G., and P. Klein, 2009: Available potential energy diagnosis in a direct numerical simu-
742 lation of rotating stratified turbulence. Cambridge University Press, 45-55 pp., [https://doi.org/](https://doi.org/10.1017/S0022112008004473)
743 [10.1017/S0022112008004473](https://doi.org/10.1017/S0022112008004473).
- 744 Rudnick, D. L., and R. Ferrari, 1999: Compensation of horizontal temperature and salinity
745 gradients in the ocean mixed layer. *Science*, **283** (5401), 526–529.
- 746 Rudnick, D. L., and J. P. Martin, 2002: On the horizontal density ratio in the upper ocean. *Dynamics*
747 *of atmospheres and oceans*, **36** (1-3), 3–21.
- 748 Scotti, A., and P. Y. Passaglia, 2019: Diagnosing diabatic effects on the available energy of
749 stratified flows in inertial and non-inertial frames. *Journal of Fluid Mechanics*, **861**, 608–642,
750 <https://doi.org/10.1017/jfm.2018.915>.
- 751 Scotti, A., and B. White, 2014: Diagnosing mixing in stratified turbulent flows with a locally
752 defined available potential energy. *Journal of Fluid Mechanics*, **740**, 114–135, [https://doi.org/](https://doi.org/10.1017/jfm.2013.643)
753 [10.1017/jfm.2013.643](https://doi.org/10.1017/jfm.2013.643).
- 754 Seo, H., A. J. Miller, and J. R. Norris, 2016: Eddy-wind interaction in the California Current Sys-
755 tem: Dynamics and impacts. *Journal of Physical Oceanography*, **46**, 439–459, [https://doi.org/](https://doi.org/10.1175/JPO-D-15-0086.1)
756 [10.1175/JPO-D-15-0086.1](https://doi.org/10.1175/JPO-D-15-0086.1).
- 757 Seo, H., and Coauthors, 2023: Ocean mesoscale and frontal-scale ocean–atmosphere interactions
758 and influence on large-scale climate: A review. *Journal of Climate*, **36** (7), 1981–2013.
- 759 Shao, M., and Coauthors, 2019: The variability of winds and fluxes observed near submesoscale
760 fronts. *Journal of Geophysical Research: Oceans*, **124**, 7756–7780, [https://doi.org/10.1029/](https://doi.org/10.1029/2019JC015236)
761 [2019JC015236](https://doi.org/10.1029/2019JC015236).
- 762 Shchepetkin, A. F., 2015: An adaptive, courant-number-dependent implicit scheme for vertical
763 advection in oceanic modeling. *Ocean Modelling*, **91**, 38–69.
- 764 Shchepetkin, A. F., and J. C. McWilliams, 2005: The regional oceanic modeling system (ROMS): A
765 split-explicit, free-surface, topography-following-coordinate oceanic model. *Ocean modelling*,
766 **9** (4), 347–404.

- 767 Skamarock, W. C., and Coauthors, 2019: A description of the advanced research wrf model version
768 4. *National Center for Atmospheric Research: Boulder, CO, USA*, **145 (145)**, 550.
- 769 Skyllingstad, E. D., D. Vickers, L. Mahrt, and R. Samelson, 2007: Effects of mesoscale sea-surface
770 temperature fronts on the marine atmospheric boundary layer. *Boundary-layer meteorology*, **123**,
771 219–237.
- 772 Small, R. J., and Coauthors, 2008: Air-sea interaction over ocean fronts and eddies. *Dynamics of*
773 *Atmospheres and Oceans*, **45**, 274–319, <https://doi.org/10.1016/j.dynatmoce.2008.01.001>.
- 774 Stewart, K. D., J. A. Saenz, A. M. C. Hogg, G. O. Hughes, and R. W. Griffiths, 2014: Effect of
775 topographic barriers on the rates of available potential energy conversion of the oceans. *Ocean*
776 *Modelling*, **76**, 31–42, <https://doi.org/10.1016/j.ocemod.2014.02.001>.
- 777 Su, Z., H. Torres, P. Klein, A. F. Thompson, L. Siegelman, J. Wang, D. Menemenlis, and C. Hill,
778 2020: High-frequency submesoscale motions enhance the upward vertical heat transport in
779 the global ocean. *Journal of Geophysical Research: Oceans*, **125**, [https://doi.org/10.1029/](https://doi.org/10.1029/2020JC016544)
780 [2020JC016544](https://doi.org/10.1029/2020JC016544).
- 781 Su, Z., J. Wang, P. Klein, A. F. Thompson, and D. Menemenlis, 2018: Ocean submesoscales
782 as a key component of the global heat budget. *Nature Communications*, **9**, [https://doi.org/](https://doi.org/10.1038/s41467-018-02983-w)
783 [10.1038/s41467-018-02983-w](https://doi.org/10.1038/s41467-018-02983-w).
- 784 Sullivan, P. P., J. C. McWilliams, J. C. Weil, E. G. Patton, and H. J. Fernando, 2020: Marine
785 boundary layers above heterogeneous SST: Across-front winds. *Journal of the Atmospheric*
786 *Sciences*, **77 (12)**, 4251–4275.
- 787 Sullivan, P. P., J. C. McWilliams, J. C. Weil, E. G. Patton, and H. J. Fernando, 2021: Marine bound-
788 ary layers above heterogeneous SST: Alongfront winds. *Journal of the Atmospheric Sciences*,
789 **78 (10)**, 3297–3315.
- 790 Tseng, Y. H., and J. H. Ferziger, 2001: Mixing and available potential energy in stratified flows.
791 *Physics of Fluids*, **13**, 1281–1293, <https://doi.org/10.1063/1.1358307>.
- 792 Valcke, S., 2013: The OASIS3 coupler: A European climate modelling community software.
793 *Geoscientific Model Development*, **6 (2)**, 373–388.

- 794 von Storch, J.-S., C. Eden, I. Fast, H. Haak, D. Hernández-Deckers, E. Maier-Reimer, J. Marotzke,
795 and D. Stammer, 2012: An estimate of the Lorenz energy cycle for the World Ocean based
796 on the 1/10° STORM/NCEP simulation. *Journal of Physical Oceanography*, **42**, 2185–2205,
797 <https://doi.org/10.1175/JPO-D-12-079.1>.
- 798 Wenegrat, J. O., 2023: The current feedback on stress modifies the Ekman buoyancy flux at fronts.
799 *Journal of Physical Oceanography*, **53** (12), 2737–2749.
- 800 Wenegrat, J. O., and R. S. Arthur, 2018: Response of the atmospheric boundary layer to sub-
801 mesoscale sea surface temperature fronts. *Geophysical Research Letters*, **45**, 13,505–13,512,
802 <https://doi.org/10.1029/2018GL081034>.
- 803 Wenegrat, J. O., and M. J. McPhaden, 2016: Wind, Waves, and Fronts: Frictional Effects in a
804 Generalized Ekman Model. *Journal of Physical Oceanography*, **46** (2), 371–394, [https://doi.org/](https://doi.org/10.1175/JPO-D-15-0162.1)
805 [10.1175/JPO-D-15-0162.1](https://doi.org/10.1175/JPO-D-15-0162.1), URL [http://journals.ametsoc.org/doi/abs/10.1175/JPO-D-15-0162.](http://journals.ametsoc.org/doi/abs/10.1175/JPO-D-15-0162.1)
806 1.
- 807 Wenegrat, J. O., L. N. Thomas, J. Gula, and J. C. McWilliams, 2018: Effects of the submesoscale
808 on the potential vorticity budget of ocean mode waters. *Journal of Physical Oceanography*,
809 **48** (9), 2141–2165.
- 810 Winters, K. B., and R. Barkan, 2013: Available potential energy density for boussinesq fluid flow.
811 *Journal of Fluid Mechanics*, **714**, 476–488, <https://doi.org/10.1017/jfm.2012.493>.
- 812 Winters, K. B., P. N. Lombard, J. J. Riley, and E. A. D’Asaro, 1995: Available potential energy and
813 mixing in density-stratified fluids. *Journal of Fluid Mechanics*, **289**, 115–128, [https://doi.org/](https://doi.org/10.1017/S002211209500125X)
814 [10.1017/S002211209500125X](https://doi.org/10.1017/S002211209500125X).
- 815 Yang, H., and Coauthors, 2024: Observations reveal intense air-sea exchanges over submesoscale
816 ocean front. *Geophysical Research Letters*, **51** (2), e2023GL106 840.
- 817 Yang, Y., J. C. McWilliams, X. S. Liang, H. Zhang, R. H. Weisberg, Y. Liu, and D. Menemenlis,
818 2021: Spatial and temporal characteristics of the submesoscale energetics in the gulf of mexico.
819 *Journal of Physical Oceanography*, **51**, 475–489, <https://doi.org/10.1175/JPO-D-20-0247.1>.

- 820 Zemsikova, V. E., B. L. White, and A. Scotti, 2015: Available potential energy and the general
821 circulation: Partitioning wind, buoyancy forcing, and diapycnal mixing. *Journal of Physical*
822 *Oceanography*, **45**, 1510–1531, <https://doi.org/10.1175/JPO-D-14-0043.1>.
- 823 Zhai, X., and R. J. Greatbatch, 2006: Surface eddy diffusivity for heat in a model of the northwest
824 Atlantic Ocean. *Geophysical research letters*, **33** (24).